Title:

Tetanus neurotoxin sensitive SNARE-mediated glial signaling limits motoneuronal excitability

Running title: Glial cells suppress motoneuronal hyperactivity

Authors

Mathias A. Böhme*, Anthony W. McCarthy, Monika Berezeckaja, Kristina Ponimaskin and Alexander M. Walter*

Affiliation

Leibniz-Forschungsinstitut für Molekulare Pharmakologie (FMP), FMP im CharitéCrossOver, 10117 Berlin, Germany.

ORCID identifier: Mathias A. Böhme: orcid.org/0000-0002-0947-9172; Anthony W. McCarthy: orcid.org/0000-0002-3771-351X; Alexander M. Walter: orcid.org/0000-0001-5646-4750

*Correspondence to: Alexander M. Walter (awalter@fmp-berlin.de) or Mathias A. Böhme (boehme@fmp-berlin.de).

Editorial correspondence to:

awalter@fmp-berlin.de

Dr. Alexander M. Walter

Molecular and Theoretical Neuroscience, Leibniz-Forschungsinstitut für Molekulare Pharmakologie, Charité Campus Mitte, Charitéplatz 1, 10117 Berlin Germany

Tel.: +49 (0)30-450-639-026

Final character count (title page, abstract and main text with spaces): 24833

Abstract

Peripheral nerves contain motoneuron axons coated by glial cells, which essentially contribute to nerve function. How glial cells communicate with other cells and whether secretion or SNARE-mediated fusion reactions are involved remains poorly understood. We here report on essential SNARE-mediated reactions in distinct glial subtypes of *Drosophila* peripheral nerves that establish insulating septate junctions (SJ) and provide metabolic support to neuronal axons. Interference with these reactions by glial expression of the proposedly neurospecific tetanus neurotoxin light chain caused nerve disintegration, interfered with axonal transport, induced tetanic muscle hyperactivity and lethal paralysis. We identify non-neuronal Synaptobrevin as the relevant vesicular SNARE protein and link its function to two glial subtypes that differentially contribute to SJ formation (subperineurial glia) and neural metabolic support (wrapping glia). Our study thus identifies a crucial role of SNARE-mediated reactions in glial subtypes for nerve function and pathology, animal motility and survival.

Key words: glia biology / SNAREs / neural excitability / septate junction / glia-neuron metabolic coupling

Introduction

Motor control is mediated by motoneurons of the central nervous system that can convey electrical information in the form of action potentials (APs) along their axons over large distances to peripheral body muscles. At the target muscle, motoneuronal APs induce the release of neurotransmitters at the neuromuscular junction (NMJ), leading to muscle excitation and contraction (Kuo & Ehrlich, 2015). Motoneuronal axons are bundled in nerves which also contain non-neuronal glial cells that separate motoneuron axons from the surrounding environment and additionally serve essential functions in development, regeneration, neural metabolism, ion homeostasis and AP propagation (Fields, 2015; Simard & Nedergaard, 2004; Zuchero & Barres, 2015)**.** The functional importance of proper neural communication along peripheral nerves is evident from the many, often fatal diseases in which this is disrupted, including Charcot–Marie–Tooth disease, Guillain-Barré syndrome**,** amyotrophic lateral sclerosis and tetanus (Bleck, 1989; Hardiman *et al*, 2017; Szigeti & Lupski, 2009; Willison *et al*, 2016).

The release of chemical transmitters, but also the delivery of proteins and lipids to different intracellular compartments depends on the fusion of cargo-containing vesicles with their target organelles. These fusion reactions are mediated by the formation of heat stable, coiled-coil soluble N-ethylmaleimide-sensitive-factor attachment receptor (SNARE) complexes between SNARE proteins resident on vesicle (v-SNARE) and target (t-SNARE) membranes (Bruns & Jahn, 2002; Jahn & Fasshauer, 2012; Jahn & Scheller, 2006). Synaptic transmission requires the fusion of neurotransmitter (NT) containing synaptic vesicles (SVs) with the plasma membrane which engages the evolutionarily conserved t-SNAREs syntaxin-1 and SNAP25 and the v-SNARE Synaptobrevin-2/VAMP2 (Syb2) in mammals or neuronal Synaptobrevin (nSyb) in *Drosophila* (DiAntonio *et al*, 1993; Jahn & Fasshauer, 2012). Tetanus neurotoxin (TeNT) is a potent bacterial toxin that abolishes NT release by TeNT-light chain (TeNT-LC) mediated cleavage of Syb-2/nSyb (Bruns *et al*, 1997; Schiavo *et al*, 1992;

Schiavo *et al*, 2000; Sweeney *et al*, 1995) while the TeNT-heavy chain (TeNT-HC) targets the NT release abolishment to inhibitory interneurons of the vertebrate spinal cord (Blum *et al*, 2012; Blum *et al*, 2014; Bomba-Warczak *et al*, 2016; Deinhardt *et al*, 2006; Deinhardt & Schiavo, 2005; Erdmann *et al*, 1975; Lalli *et al*, 2003; Rummel, 2017; Schiavo *et al.*, 2000; Schwab & Thoenen, 1976, 1978; Surana *et al*, 2018; Yeh *et al*, 2010). The resulting loss of inhibitory input onto spinal motoneurons causes hyperactivity, spastic paralysis and ultimately respiratory failure and death (Bleck, 1989; Popoff & Poulain, 2010; Surana *et al.*, 2018). Despite the availability of functional vaccines, Tetanus still caused ~25000 death children in 2018 (Source: www.who.int) making a complete functional understanding of this disease essential. Interestingly, also glial cells, including the nerve-isolating peripheral Schwann cells, can take up TeNT (Huba & Hofmann, 1988; Schwab & Thoenen, 1978) and glial TeNT expression or disruption of its v-SNARE targets (VAMP2/Syb-2, VAMP3/cellubrevin) affects the function of central neurons (Lee *et al*, 2014; Pascual *et al*, 2005; Perea & Araque, 2007; Schwarz *et al*, 2017). However, whether TeNT in glial cells may affect motoneuroal function or even contribute to tetanus pathology remains unknown.

We here report on the unexpected observation that TeNT-LC expression in *Drosophila* glial cells severely disrupts peripheral nerve morphology and axonal transport of synaptic material. It furthermore caused motoneuronal hyperactivity and paralysis, typical effects of TeNT intoxication in higher organisms. Unlike neurons, where TeNT-LC cleaves nSyb and arrests neurotransmission, in glial cells these effects were caused by the functional loss of non-neuronal Syb. TeNT-LC expression in axon encircling wrapping glia caused an axonal accumulation of the synaptic protein Bruchpilot (BRP). Similar effects were observed when knocking down Basigin, a protein that targets monocarboxylate transporters to plasma membranes, suggesting a defect in metabolic supply to neurons. In contrast, TeNT-LC (or Syb-RNAi) expression in subperineurial glial cells additionally disrupted nerve morphology as well as septate junction formation and in some cases caused nerve hyperactivity. In

conclusion we report on SNARE-mediated reactions in glial cells that are essential for motor function and whose disruption may cause severe pathology, including tetanus.

Results and discussion

Expression of TeNT-LC in glial cells disrupts nerve morphology and function

Classic experiments revealed TeNT uptake also into Schwann cells (Schwab & Thoenen, 1978) and glial cells exocytose substances influencing motor function possibly in a SNARE-dependent manner (Carlsen & Perrier, 2014; Christensen *et al*, 2018; Christensen *et al*, 2013; Gucek *et al*, 2012; Schwarz *et al.*, 2017). We therefore wondered whether TeNT-LC targeted to glial cells could also affect motoneural function, or even contribute to tetanus pathology.

Three types of *Drosophila* glial cells are found in a compound organization coating the segmentally arranged abdominal peripheral nerves (Bittern *et al*, 2020; Stork *et al*, 2008) and Fig. 1A,B), which harbor the sensory- and motoneuron axons (motoneuronal innervation depicted in Fig 1B, left). We started our investigation by expressing TeNT-LC (Sweeney *et al.*, 1995)) specifically in all glial subtypes using the pan-glial driver Repo-Gal4 and investigated the influence on larval behavior, peripheral nerve morphology (via staining with horse-radish peroxidase (HRP) as neuronal membrane marker) and function (Fig. 1C-H). Surprisingly, pan-glial TeNT-LC expressing larvae were severely paralyzed, hardly able to move and died at late larval stages (Fig 1C,D and Video 1-3), thus showing typical hallmarks of TeNT intoxication. Additionally, peripheral nerves of pan-glial TeNT-LC expressing larvae showed severely disrupted integrity including a partial defasciculation (Fig. 1E, arrow head for single axon leaving the nerve trunk) and an expansion of the nerve area (Fig. 1E,F). A recent study reported similar, but locally constrained nerve swellings upon glial knock-down (KD) of the salt-inducible kinase 3 (SIK3), a central node in a signal transduction pathway controlling glial K^+ and water homeostasis (Li *et al*, 2019). In contrast, peripheral nerves of pan-glial TeNT-LC expressing animals showed a continuous disruption of the entire axonal length although to different degrees. We quantitatively evaluated the severity of the disruption by categorizing the nerves by their degree of disintegration (normal: long, thin and smooth nerves (see control images in Fig. 1E for example); intermediate: slight morphological

alterations like single defasciculating axons, slightly increased nerve area; disrupted: complete disintegration of the nerve, defasciculation of whole parts of the nerve, large expansion of the nerve area). While control groups (larvae with either the Repo-Gal4 driver or the UAS-TeNT-LC construct alone) almost exclusively showed normal nerve morphologies, most nerves expressing pan-glial TeNT-LC were disrupted (Fig. 1F). Additionally, pan-glial TeNT-LC expression caused a five-fold increase in the number of spots in the axon containing presynaptic protein BRP (labelled by immunostaining; Fig 1E,F).

Peripheral nerves contain motoneurons that finally submerge into the *Drosophila* body wall muscles to form neuromuscular junctions (NMJs; Fig. 1B) whose action potential (AP) evoked activation enables muscle contraction and larval movement. We continued investigating the functional influence of glial TeNT-LC action on spontaneous and AP-evoked synaptic transmission by performing current clamp recordings (Fig. 1G,H). Amplitudes of spontaneous (miniature) excitatory postsynaptic potential (mEPSPs) were almost doubled upon pan-glial TeNT-LC expression in comparison to controls (Fig. 1G,H) while the frequency of these events were similar (*Repo*::+: 2.054 ± 0.1678 Hz, *TeNT-LC*::+: 2.538 ± 0.2536 Hz, *Repo*::*TeNT-LC*: 1.874 ± 0.1812 Hz; one-way ANOVA with Tukey's multiple comparison test, *Repo*::+ vs. *TeNT-LC*::+: $p = 0.226$, *Repo::+* vs. *Repo*::*TeNT-LC*: $p = 0.8009$, *TeNT-LC::+* vs. *Repo*::*TeNT-LC*: $p = 0.0837$). In control motor axons a single stimulation evokes a single AP that reliably triggered a single excitatory postsynaptic potential (eEPSP; seen in 8/8 driver control and 7/7 TeNT-LC-construct control cells; Fig. 1G,H). In contrast, upon pan-glial TeNT-LC expression, a single stimulus triggered abnormal additional eEPSPs and thus motoneuronal hyperactivity (ranging from 2 to 246 additional events per cell, seen in 10/10 cells; Fig. 1G,H), a typical hallmark of TeNT intoxication in higher organisms. This is a similar observation to one seen with glial-KD of SIK3, although in that case supernumerary EPSPs also occurred without any stimulation(Li *et al.*, 2019). While the number of eEPSPs elicited per stimulus was increased, the average

amplitude of the first eEPSPs we observed did not differ from control cells (Fig. 1G,H). Thus, we report that TeNT-LC-mediated interference with SNARE-dependent processes in glial cells impairs axonal transport, disrupts nerve integrity, causes motoneural hyperexcitability, and paralysis.

Essential glial functions are mediated by Syb but not nSyb

We next asked which v-SNARE might be targeted by TeNT-LC in glial cells (Fig. 2A). Tetanus pathology is caused by Synaptobrevin-2 cleavage in mammalian interneurons (Schiavo *et al.*, 2000). However, TeNT-LC also cleaves other v-SNAREs, including VAMP1/Synaptobrevin-1 enriched in spinal cord neurons and the more ubiquitously expressed VAMP3/cellubrevin in mammals (Carle *et al*, 2017; Elferink *et al*, 1989; McMahon *et al*, 1993; Patarnello *et al*, 1993; Schiavo *et al.*, 1992). The *Drosophila* genome harbors two putative TeNT-LC targets, neuronal-Synaptobrevin (nSyb) involved in the fusion of SVs (Deitcher *et al*, 1998; DiAntonio *et al.*, 1993; Sweeney *et al.*, 1995) and synaptobrevin (Syb) which is rather ubiquitously expressed and likely involved in more constitutive vesicular fusion reactions (Chin *et al*, 1993; Sudhof *et al*, 1989). TeNT-LC was originally thought to specifically cleave *Drosophila* nSyb (Sweeney *et al.*, 1995). However, an alignment of nSyb and non-neuronal Syb revealed differences mainly in their N- and C-terminal parts while the central SNARE-motif (Fig. 2B, yellow shaded) is largely conserved (Fig. 2B). Importantly, the glutamine (Q) – phenylalanine (F) TeNT-LC-cleavage site (Schiavo *et al.*, 1992), is conserved in both proteins (Fig 2B, red box). We thus investigated the influence of nSyb or Syb knock-down (KD) on glial cells by expressing specific RNAi lines using Repo-Gal4 (Fig. 2C-H). Pan-glial nSyb knock-down showed no change in nerve morphology, nerve area or on axonal BRP presence in comparison to controls (Fig. 2C,D; similar results were obtained with a second nSyb-RNAi line (#VDRC 49201, data not shown)). In contrast, pan-glial knockdown of non-neuronal Syb phenocopied pan-glial TeNT-LC expression with largely increased nerve

areas, severely disrupted nerve morphologies and enhanced axonal BRP accumulations (Fig. 2E,F). Similarly to glial TeNT-LC expression, mEPSP amplitudes were increased and cells exhibited hyperactive motoneuronal behavior with supernumerary eEPSPs after stimulation (ranging from 2 to 62 additional events per cell, seen in 9/10 cells; Fig. 2G,H). Evoked amplitudes of the first eEPSP after stimulation remained unchanged (Fig. 2G,H). Thus, TeNT-LC-mediated impairment of Syb- and not nSyb-function in *Drosophila* glial cells is likely responsible for disrupted nerve integrity, axonal accumulation of synaptic proteins and hyperactive motoneuronal responses.

<u>TeNT-LC expression in SPGs causes nerve disintegration, disrupts axonal transport and can result in hyperactivity</u>

We next speculated how TeNT-LC or Syb-KD cause these phenotypes and whether all glial subtypes are affected. *Drosophila* peripheral axons are supported by three glial types: wrapping glia (WGs), subperineurial glia (SPGs) and perineurial glia (PGs) ((Stork *et al.*, 2008) and Fig. 1B). SPG enwrap axons and WG ((Stork *et al.*, 2008) and Figs. 1B & 3A) and additionally extend to completely cover the NMJ in 35% of cases (investigated using rl82-Gal4 (Gli-Gal4 (Auld *et al*, 1995; Sepp & Auld, 1999)) mediated expression of membrane associated GFP (mCD8-GFP); Fig. 3B,C), in line with previous results (Auld *et al.*, 1995; Brink *et al*, 2009; Fuentes-Medel *et al*, 2009; Kerr *et al*, 2014; Sepp & Auld, 1999). Similarly to pan-glial TeNT expression (Fig. 1C,D and Videos 1-3) also SPG TeNT-LC expressing larvae were severely paralyzed, showing uncoordinated movement, and died at pupal stages (Fig. EV1A,B and Videos 2,4,5). However, in the course of this study we also found two rare adult escapees of TeNT-LC expressing SPGs. These flies were also severely paralyzed, showed almost no movement and were even unable to re-orientate to an upright stance when falling on their back (Video 6). Furthermore and similarly to pan-glial TeNT-LC/Syb-RNAi expression, TeNT-LC expression specifically in SPGs caused disrupted nerve morphology,

enlarged nerve area, axonal BRP accumulations and occasionally showed aberrant hyperactive motoneuronal responses after AP-evoked stimulation, though this effect was weaker than upon pan-glial expression (2 to 42 additional events per cell, seen in 3/10 cells but in none of the control conditions; compare Fig. 3D-G with Fig. 1C-F and Fig. 2E-H). Expression of TeNT-LC in SPG in some cases also caused failures to stimulate eEPJPs (seen in 2/10 cells; Fig. 3G) and did not increase mEPSP amplitudes (Fig. 3F,G; in contrast to pan-glial TeNT-LC expression (Fig. 1E,F)). The generally milder effects might be due to the additional contribution of other glial cell types or due to a weaker expression strength of the rL82-Gal4 driver compared to Repo-Gal4 (Yildirim *et al*, 2019).

Despite disrupted nerves, TeNT-LC expression is unlikely to kill SPGs cells as simultaneous CD8-GFP expression showed an intact GFP coverage of investigated nerves similar to control cells (Fig. EV1C,D). We further confirmed that Syb but not nSyb was the TeNT-LC target in SPGs as KD of Syb did not kill SPGs but elicited similar effects as SPG TeNT-LC or pan-glial Syb-RNAi expression (compare Fig. EV1E,F and Fig. EV2A-G with Figs. 1E-H; 2E-H and 3D-G). Interestingly, while mEPSP amplitudes were unchanged upon SPG Syb-RNAi expression, AP-evoked amplitudes were increased (Fig. EV2D,E), a phenotype we did not discover previously via pan-glial TeNT-LC/Syb-RNAi expression nor by SPG TeNT-LC expression (Figs. 1G,H; 2G,H and 3F,G). As a marginal note, staining peripheral nerves with an antibody against the glutamate receptor subunit IID (Qin *et al*, 2005), reliably labelled an outer layer of the nerve, possibly the neural lamella. In SPG Syb-RNAi expressing larvae, extensive folds of this lamellar area in addition to large “voids” within the axonal HRP staining became obvious (Fig. EV2A,B; neural lamella). Staining for two other obligatory GluR subunits, GluRIIA nor GluRIIB (Petersen *et al*, 1997; Qin *et al.*, 2005; Schuster *et al*, 1991) showed no nerve staining (data not shown), suggesting that nerve GluRIID staining labels an unidentified, unspecific epitope which nonetheless may be useful

for analysis. The embryonic lethality of *gluRIID*^{Null} mutants (Qin *et al.*, 2005) occludes further investigation.

We next wondered what biological processes may be disrupted upon TeNT-LC expression in SPGs. The morphological nerve phenotypes we discovered (disintegration, enlarged nerve area, "voids") are comparable to previously reported phenotypes of mutants interfering with septate junction (SJ) formation or failures of the ensheathing glia to correctly wrap peripheral axons (Babatz *et al*, 2018; Leiserson *et al*, 2000). SJs seal off the axon/WG bundles encircling SPGs (Fig 1B, right) to build an occluding barrier that establishes metabolic insulation (Banerjee *et al*, 2008; Baumgartner *et al*, 1996; Carlson *et al*, 2000; Schwabe *et al*, 2005; Stork *et al.*, 2008; Yildirim *et al.*, 2019). As exocytosis reactions are thought to play a role in SJ establishment (Babatz *et al.*, 2018; Tiklova *et al*, 2010) we wondered whether TeNT-LC/Syb-RNAi expression interfered with SJ formation in SPGs and expressed TeNT-LC together with an endogenously GFP-tagged version of NrxIV-GFP, an essential SJ component (Babatz *et al.*, 2018; Baumgartner *et al.*, 1996; Oshima & Fehon, 2011; Stork *et al.*, 2008). In control nerves, NrxIV-GFP labelled SJs exhibit a very restricted linear arrangment along the peripheral nerves (Fig. 3H-J; note peak in vertical nerve line profil (Fig. 3H,I; top panel, solid green line) and single large GFP signal in orthogonal nerve crosse section (Fig. 3J, left). TeNT expression led to a loss of the delineted Nrx-GFP positive SJs resulting in diffuse NrxIV-GFP signal with rather flat distribution across the nerve (Fig. 3H,I bottom panels for two examples and 3J, right). To further investigate whether impaired SJ formation could cause some of the defects observed upon TeNT-LC expression, we interfered with SJ formation directly in SPGs by knocking down NrxIV. Similar to TeNT-LC/Syb-RNAi expression, NrxIV-KD in SPGs led to a strong disintegration of the nerve morphology, largely increased nerve area and a strong axonal BRP-accumulation (6-fold increase in comparison to controls; compare Fig. 3K,L with 3D,E and Fig. EV2A,B). Electrophysiological characterization of NrxIV-RNAi expressing SPGs revealed increased

mEPSP amplitudes (one-way ANOVA with Tukey's multiple comparison test: *rL82::+* vs. *rL82::NrxIV-RNAi*: p = 0.04; *NrxIV-RNAi::+* vs. *rL82::NrxIV-RNAi*: p = 0.1; *rL82::+* vs. *NrxIV-RNAi::+:* p = 0.8) and an increase of AP-evoked amplitudes (Fig. 3M,N). However, despite the morphological disruption, we did not discover any hyperactivity in NrxIV-RNAi expressing cells (Fig. 3M,N). This could either reflect the involvement of an independent component whose delivery depends on Syb or a less severe disruption of SJ formation than upon TeNT-LC/Syb-RNAi expression. Notably, the impaired blood-brain barrier function in *nrxIV* mutants is partially compensated by the formation of intertwined cell-cell protrusions, resembling an evolutionary ancient barrier type found in primitive vertebrates or invertebrates (Babatz *et al.*, 2018; Bundgaard & Abbott, 1992, 2008; Stork *et al.*, 2008) potentially sufficient to suppress hyperexcitability. Alternatively and/or additionally, TeNT-LC/Syb-RNAi expression might also impair other exocytotic processes (Hoogstraaten *et al*, 2020; Pascual *et al.*, 2005; Perea & Araque, 2007; Schwarz *et al.*, 2017). Recently, interference with WNT- and thus peptidergic-signaling specifically in SPGs was shown to affect postsynaptic glutamate receptors and synaptic transmission (Kerr *et al.*, 2014). Indeed, Syb-RNAi expression in SPGs caused an accumulation of the peptidergic vesicle marker atrial natriuretic peptide (ANF (Rao *et al*, 2001); 11-fold increase in comparison to control; Fig. EV2H,I) suggesting that peptidergic release from SPG is mediated by Syb, which might also be blocked by TeNT-LC expression and contribute to the effects on nerve function.

<u>TeNT-LC expression in WG impairs axonal transport</u>

SPG cells are not in direct contact with peripheral axons after early larval stages (Fig. 1B and (Stork *et al.*, 2008)). We thus wondered whether the influence of SPGs on axonal transport might be indirect and rather via WGs whose functionality might also be impaired when nerve integration or signaling from the SPGs is disrupted. Although WGs directly contact axons/axon bundles, they rarely extend to the NMJ and we did not observed them to fully

cover it (Fig. 4A-C). TeNT-LC expression in WGs using the WG-specific Nrv2-Gal4 driver line (although expression of Nrv2-Gal4 in cortex glia was also reported, which, however, are not present at peripheral nerves (Stork *et al.*, 2008; Yildirim *et al.*, 2019)) did not kill WG cells examined via simultaneous CD8-GFP expression (Fig. EV3A,B). Unlike TeNT-LC expression in SPGs, TeNT-LC expression in WGs neither disrupted nerve integrity nor altered nerve area but caused a similarly strong accumulation of axonal BRP (Fig. 4D,E). Thus, axonal accumulation of synaptic BRP can be genetically uncoupled from the nerve defasciculation and hyperexcitablity described above. Accordingly, the none-additive nature of the effects could imply that axonal BRP accumulations observed upon SPG-perturbation (Figs. 3D,E,K,L; Fig. EV2A,C) may be caused by an indirect interference with WG function.

Glial cells support axonal mitochondrial energy metabolism (Edgar *et al*, 2009; Edgar *et al*, 2004; Griffiths *et al*, 1998; Nave, 2010) and we hypothesized that impaired axonal transport may reflect poor energy supply. We investigated whether this was disrupted by TeNT-LC comparing our phenotype to that of Basigin KD, an essential component of the metabolic alanine and lactate neuron to glia shuttle (Funfschilling *et al*, 2012; Halestrap & Wilson, 2012; Lee *et al*, 2012; Liu *et al*, 2017; Machler *et al*, 2016; Nakai *et al*, 2006; Pierre & Pellerin, 2005). Indeed and reminiscent of the effects observed upon TeNT-LC expression in WGs, WG specific expression of Basigin-RNAi led to a strong accumulation of axonal BRP (6-fold increase, Fig. 4F,G, slightly stronger than WG TeNT-LC: ~3-fold (Fig. 4D,E)) without any effect on axonal area, nerve integrity or neuronal lamella (Fig. 4F,G; Fig. EV3C-E). Thus TeNT-LC might interfere with Syb-mediated energetic support of axonal transport in WGs. Additionally, Basigin-KD in SPGs was without effect (Fig. EV3F,G), further consistent with differential influences of WGs and SPGs in the support of axonal function.

In conclusion we found unexpected and profound effects of TeNT-LC action on distinct glial cell types causing motoneuronal hyperexcitability and paralysis, and thus typical signs of TeNT-LC intoxication in mammals. Additionally we discovered disintegration of

nerve morphology, disruption of SJs, glial accumulation of peptidergic vesicles and impaired axonal transport. The observed phenotypes open new research avenues on how SNARE-mediated reactions in glial cells support neurons and other glial cells for proper nervous system function and whether disruptions of these contribute to diseases of peripheral motor control, including tetanus.

Material and methods

Fly husbandry, stocks and handling

Fly strains were reared under standard laboratory conditions (Sigrist *et al*, 2003) and raised at 25°C on semi-defined medium (Bloomington recipe). For RNAi experiments larvae were kept at 29°C. For experiments both male and female 3rd instar larvae were used. The following genotypes were used: Figure 1 and Videos 1-3: Wild-type: +/+ (w^{1118}). Repo::+: *Repo-Gal4/+*; TeNT-LC::+: *UAS-TeNT-LC/+*; Repo::TeNT-LC: *Repo-Gal4/UAS-TeNT-LC*. Figure 2: Repo::+: *Repo-Gal4/+*; nSyb-RNAi::+: *UAS-nSyb-RNAi/+*; Repo::nSyb-RNAi: *UAS-nSyb-RNAi/+;Repo-Gal4/+*; Syb-RNAi: *UAS-Syb-RNAi/+*; Repo::Syb-RNAi: *UAS-Syb-RNAi/+;Repo-Gal4/+*. Figure 3, Videos 4, 5: rL82::CD8-GFP: *rL82-Gal4/+; UAS-mCD8-GFP/+*; rL82::+: *rl82-Gal4/+*; TeNT-LC::+: *UAS-TeNT-LC/+*; rL82::TeNT-LC: *rL82-Gal4/+;UAS-TeNT-LC/+*; rL82::NrxIV-GFP: *rl82-Gal4/+; NrxIV::GFP*^{454}*/+*; rL82::NrxIV-GFP::TeNT-LC: *rl82-Gal4/+; NrxIV::GFP*^{454}*/UAS-TeNT-LC*; NrxIV-RNAi::+: *UAS-NrxIV-RNAi/+*; rL82::NrxIV-RNAi: *rL82-Gal4/UAS-NrxIV-RNAi*. Video 6: rL82::TeNT-LC: *rL82-Gal4/(Wim); UAS-TeNT-LC/+*; Control: w1118. Figure 4: Nrv2::CD8-GFP: *Nrv2-Gal4/+; UAS-mCD8-GFP/+*; Nrv2::+: *Nrv2-Gal4/+*; TeNT-LC::+: *UAS-TeNT-LC/+*; Nrv2::TeNT-LC: *Nrv2-Gal4/+;UAS-TeNT-LC/+*; Basigin-RNAi::+: *UAS-Basigin-RNAi/+*; Nrv2::Basigin-RNAi: *Nrv2-Gal4/+;UAS-Basigin-RNAi/+*. Fig. EV1: rL82::+: *rl82-Gal4/+*; TeNT-LC::+: *UAS-TeNT-LC/+*; rL82::TeNT-LC: *rL82-Gal4/+;UAS-TeNT-LC/+*; rL82::CD8-GFP: *rL82-Gal4/+; UAS-mCD8-GFP/+*; rL82::CD8-GFP::TeNT-LC: *rL82-Gal4/+; UAS-mCD8-GFP/UAS-TeNT-LC*; rL82::CD8-GFP: *rL82-Gal4/+; UAS-mCD8-GFP/+*; rL82::CD8-GFP::Syb-RNAi: *rL82-Gal4/Syb-RNAi; UAS-mCD8-GFP/+*. Fig. EV2: rL82::+: *rl82-Gal4/+*; Syb-RNAi::+: *UAS-Syb-RNAi/+*; rL82::Syb-RNAi: *rL82-Gal4/UAS-Syb-RNAi*; nSyb-RNAi::+: *UAS-nSyb-RNAi/+*; rL82::nSyb-RNAi: *rL82-Gal4/UAS-nSyb-RNAi;* rL82::ANF-EMD: *rL82-Gal4/+; UAS-ANF-EMD/+*; rL82::ANF-EMD::Syb-RNAi: *rL82-Gal4/Syb-RNAi; UAS-ANF-EMD/+*. Fig. EV3: Nrv2::CD8-GFP: *Nrv2-Gal4/+; UAS-mCD8-*

GFP/+; Nrv2::CD8-GFP::TeNT-LC: *Nrv2-Gal4/+; UAS-mCD8-GFP/UAS-TeNT-LC*; Basigin-RNAi::+: *UAS-Basigin-RNAi/+*; Nrv2::Basigin-RNAi: *Nrv2-Gal4/+;UAS-Basigin-RNAi/+*; rL82::+: *rL82-Gal4/+*; Basigin-RNAi::+: *UAS-Basigin-RNAi/+*; rL82::Basigin-RNAi: *rL82-Gal4/+;UAS-Basigin-RNAi/+*.

Stocks were obtained from: Repo-Gal4 (Sepp *et al*, 2001); UAS-TeNT-LC (Sweeney *et al.*, 1995); UAS-nSyb-RNAi (VDRC #104531/#49201); UAS-Syb-RNAi (VDRC #102922); rL82-Gal4 (Sepp & Auld, 1999); Nrv2-Gal4 (Sun *et al*, 1999); NrxIV::GFP^{454} (Edenfeld *et al*, 2006); UAS-mCD8-GFP (Lee & Luo, 1999); UAS-Basigin-RNAi (VDRC #43307); UAS-NrxIV-RNAi (VDRC #8353); UAS-ANF-EMD (Rao *et al.*, 2001).

Immunostaining

Third-instar w1118 larvae were put on a dissection plate with both ends fixed by fine pins. Larvae were then covered by 50 µl of ice-cold hemolymph-like saline solution (HL3, pH adjusted to 7.2 (Stewart *et al*, 1994): 70 mM NaCl, 5 mM KCl, 20 mM MgCl2, 10 mM NaHCO3, 5 mM Trehalose, 115 mM D-Saccharose, 5 mM HEPES). Using dissection scissors a small cut at the dorsal, posterior midline of the larva was made from where on the larvae was cut completely open along the dorsal midline until its anterior end. Subsequently, the epidermis was pinned down and slightly stretched and the internal organs and tissues removed. Care was taken not to harm the ventral nerve cord and the peripheral nerves. The dissected samples were washed 3x with ice-cold HL3 and then fixed for 5 minutes with ice-cold methanol. After fixation, samples were briefly rinsed with HL3 and then blocked for 1h in 5% native goat serum (NGS; Sigma-Aldrich, MO, USA, S2007) diluted in phosphate buffered saline (Carl Roth, Germany) with 0.05% Triton-X100 (PBT). Subsequently dissected samples were incubated with primary antibodies (mouse Nc82 = anti-BRP$^{C\text{-term}}$ (1:100, Developmental Studies Hybridoma Bank, University of Iowa, Iowa City, IA, USA; AB Registry ID: AB_2314865); rabbit BRP^{Last200} (1:1000; (Ullrich *et al*, 2015)); rabbit GluRIID

(1:500; (Qin *et al.*, 2005)); mouse GFP 3E6 (1:500, Thermo Fisher Scientific Inc., MA, USA, A-11120; AB Registry ID: AB_221568)) diluted in 5% NGS in PBT overnight. Afterwards samples were washed 5x for 30 min with PBT and then incubated for 4h with fluorescence-labeled secondary antibodies (goat anti-HRP-647 (1:500, Jackson ImmunoResearch 123-605-021, PA, USA); goat anti-rabbit-Cy3 (1:500, Jackson ImmunoResearch 111-165-144, PA, USA); goat anti-mouse-Cy3 (1:500, Jackson ImmunoResearch 115-165-146, PA, USA); anti-Phalloidin-Atto565 (1:1700; Sigma-Aldrich, MO, USA, 94072); goat anti-mouse Alexa-Fluor-488 (1:500, Life Technologies A11001, CA, USA)) diluted in 5% NGS in PBT. Samples were then washed overnight in PBT and subsequently mounted in vectashield (Vector labs, CA, USA) on microscope slides (Carl Roth, Germany; H868) and sealed with coverslips (Carl Roth, Germany, H 875). Antibodies obtained from the Developmental Studies Hybridoma Bank were created by the NICHD of the NIH and maintained at The University of Iowa, Department of Biology, Iowa City, IA 52242.

Image Acquisition, Processing, and Analysis

Confocal microscopy was performed with a Leica SP8 microscope (Leica Microsystems, Germany). Images were acquired at room temperature. Confocal imaging was done using a 63×1.4 NA oil immersion objective with a zoom of 1.8 and z-step size of 0.25 µm. All confocal images were acquired using the LAS X software (Leica Microsystems, Germany). Images from fixed samples were taken from nerve bundles exiting the ventral nerve cord of segments A2-A4 (see Figure 1A for depicted ROI). Confocal stacks were processed with ImageJ software (http://rsbweb.nih.gov/ij/). Quantifications of axonal BRP spot numbers were performed following an adjusted manual(Andlauer & Sigrist, 2012), briefly as follows. The signal of a HRP-647 antibody was used as template for a mask, restricting the quantified area to the shape of the nerve. The original confocal stacks were converted to maximal projections and a mask of the axonal BRP spots was created by applying a threshold to remove irrelevant

lower intensity pixels. The threshold was adjusted manually and individually to every image to detect all axonal BRP spots. The segmentation of single spots was done semi-automatically via the command “Find Maxima” embedded in the ImageJ software and by hand with the pencil tool and a line thickness of 1 pixel. To remove high frequency noise a Gaussian blur filter (0.5 pixel Sigma radius) was applied. The processed picture was then transformed into a binary mask using the same lower threshold value as in the first step. This binary mask was then projected onto the original unmodified image using the “min” operation from the ImageJ image calculator. BRP spot numbers and sizes were determined using the “Analyze particles” function (particle size > 2 pixels) embedded into ImageJ. Line profiles were measured using the plot profile function of ImageJ. To measure the axonal (HRP) or lamellar (GluRIID) area, the signal of the HRP-647 or the GluRIID antibody was used as template for a binary mask. The area was then quantified using the “wand tool” to select the area and “measure” function embedded into ImageJ to quantify the area. For orthogonal sections, confocal RGB stacks were processed using MATLAB R2016a as follows: first, the whole stack containing the three channels (BRP, GluRIID, HRP) was loaded using the command "imread" in a loop iterating through the first to last image of the stack. Then, the three channels were separated into three stacks for the following permutation operation. Using the command "permute", the 2nd and 3rd dimension were switched separately in each stack. Lastly, each of the three permuted stacks was written to a file using the command "imwrite" in a loop iterating through all images of the stack, resulting in three .tif-files (each for one channel) showing the orthogonal view of the imaged nerve. The respective code is available upon request. Orthogonal views of each nerve (BRP, GluRIID, HRP) were then merged using ImageJ.

To evaluated nerve disruption, nerves were manually categorized by their degree of disintegration. Category 1: normal morphology: long, thin and smooth nerves (see control images in Fig. 1E for example); category 2: intermediate: slight morphological alterations like single defasciculating axons, slightly increased nerve area; category 3: disrupted: complete

disintegration of the nerve integrity, defasciculation of whole parts of the nerve, large expansion of the nerve area (see *Repo::Syb-RNAi* image in Fig. 2E for example).

Images for figures were processed with ImageJ software to enhance brightness using the brightness/contrast function.

Video of larval and adult fly movement

Larval behavior was investigated by placing 3rd instar larvae of the correct genotype in the center of a petri dish (diameter: 5 cm) that contained two ml of water to avoid larvae attachment to the plastic dish or larvae crawling up the wall of the dish. Videos were recorded with a Samsung Galaxy A50 for ca. 90s using the imbedded video function. A ruler was placed next to the dish to allow measuring the walking distance. For analysis, videos were converted to AVI format and compressed using FFmpegTool software (v4.3, ffmpeg.zeranoe.com). Videos were analyzed by a different person than the one recording the video blinded for genotype. Using Fiji software (ImageJ 1.51n) a substack was created for each video, selecting every 50th frame. This reduced the framerate from 30 Hz to 0.6 Hz. Using the manual tracking plugin of Fiji, the head of the larva was selected and tracked in each frame of the substack for 85 s after it was added to the dish. Final larval movement tracks were saved as ROIs and the total distance travelled by each larva calculated.

For adult behavior assessment two *rL82::TeNT-LC* flies and one control (w1118) were put in an empty food vial and illuminated with a ZLED CLS 600 (Zett Optics, Gemany) light source. To induce fly movement, the vial was occasionally banged on the table.

Protein sequence alignment

Sequences of Syb-PA (ID: FBpp0087450) and nSyb-PA (ID: FBpp0072697) were obtained from flybase (flybase.org, version FB2020_02; date: May 28 2020). Alignment was performed using Clustal Omega ((Sievers *et al*, 2011);

https://www.ebi.ac.uk/Tools/msa/clustalo/; version 1.2.4). Gonnet PAM250 matrix was used to compare sequence substitutions: * identical aa, : score >0.5, . score <0.5, "gap" score below 0.

Electrophysiology

Third instar larvae were individually placed on Sylgard (184, Dow Corning, Midland, MI, USA) and pinned at the head and the tail. 40 µl modified hemolymph-like solution (HL3; (Stewart *et al.*, 1994) composition (in mM): NaCl 70, KCl 5, $MgCl_2$ 10, $NaHCO_3$ 10, trehalose 5, sucrose 115, HEPES 5, $CaCl_2$ 0, pH adjusted to 7.2) was pipetted onto the larva at room temperature (~22°C). A small incision was made with a sharp scissors in the dorsal cuticle near the tail pin. Starting from this posterior incision, a cut was made along the length of the larva extending beyond the head pin. The cuticle was pinned down twice on either side. The intestines and trachea were cut at the posterior and held firmly with a forceps as the remaining connections to the body were cut before being fully removed, taking care not to pull on the preparation. The brain was held slightly raised above the preparation and the segmental nerves cut without touching the underlying muscle, before finally removing the brain. The Sylgard block and completed larval preparation was placed in the recording chamber which was filled with 2 ml HL3 (plus 0.4 mM $CaCl_2$, 10 mM $MgCl_2$). Recordings were performed at room temperature in current clamp mode at muscle 6 in segments A2/A3 as previously described(Zhang & Stewart, 2010) using an Axon Digidata 1550A digitizer, Axoclamp 900A amplifier with HS-9A x0.1 headstage (Molecular Devices, CA, USA) and on a BX51WI Olympus microscope with a 40X LUMPlanFL/IR water immersion objective. Sharp intracellular recording electrodes were made using a Flaming Brown Model P-97 micropipette puller (Sutter Instrument, CA, USA) with a resistance of 20-35 MΩ and back-filled with 3 M KCl. Cells were only considered with a membrane potential of less than -60 mV and membrane resistances greater than 3 MΩ. All recordings were acquired using

Clampex software (v10.5), filtered with a 5 kHz low-pass filter and sampled at 10-50 kHz. eEPSPs were recorded by stimulating the appropriate nerve at 10 s intervals five times (8 V, 300 µs pulse) using an ISO-STIM 01D stimulator (NPI Electronic, Germany). Stimulating suction electrodes were pulled on a DMZ-Universal Puller (Zeitz-Instruments GmbH, Germany) and fire polished using a CPM-2 microforge (ALA Scientific, NY, USA). A maximum of two cells were recorded per animal.

Analysis was performed with Clampfit 10.5 and Graphpad Prism 6 software. mEPSPs were further filtered with a 500 Hz Gaussian low-pass filter. A single mEPSP template was generated for each 1-minute cell recording and used to identify individual mEPSPs, calculating the mean mEPSP amplitude per cell. To calculate eEPSP amplitudes, an average trace was generated from the five traces and the amplitude of the first response peak in the resulting average trace calculated. To determine hyperactivity or aberrant cell responses, a threshold was set at 8 mV. The number of response peaks above the 8 mV threshold for each cell was determined and normalized to the number of stimuli (five). Aberrant activity in a cell was defined as multiple response peaks above the 8 mV threshold following each individual stimulus, or any response to an individual stimulus below the 8 mV threshold including failures.

Quantification and Statistical Analysis

Data were analyzed using Prism (GraphPad Software, CA, USA). Per default two-sided Student's t test was performed to compare the means of two groups unless the data were non-normally distributed (as assessed D'Agostino-Pearson omnibus normality test) in which case they were compared by a two-tailed Mann-Whitney U test. For comparison of more than two groups, one-way analysis of variance (ANOVA) tests were used, followed by a Tukey's multiple comparison test. In the case of ordinal data (nerve morphology) a Kruskal-Wallis test

was used. Means are annotated ± s.e.m.. Asterisks are used to denote significance: *, $p < 0.05$; **, $p < 0.01$; ***, $p < 0.001$; n.s. (not significant), $p > 0.05$.

Data and Software Availability

The data that support the findings of this study, additional information and requests for resources and reagents as well as Matlab or ImageJ codes used in this study are available from Alexander M. Walter (awalter@fmp-berlin.de) upon request.

Acknowledgements

We thank C. Klämbt, Stephan J. Sigrist and Sean Sweeney for comments on the manuscript and C. Klämbt for NrxIV-GFP and NrxIV-RNAi fly lines. We thank Katherine Cuthill, Björn von Domarus and Christina Fefler for help with initial experiments and Björn von Domarus for help with confocal analysis. We thank Andreas T. Grasskamp for his help with the orthogonal view. This work was supported by grants from the Deutsche Forschungsgemeinschaft to A.M. Walter (Emmy Noether programme, TRR 186).

Author contributions

M.A.B and A.M.W conceived the project. M.A.B., K.P. and A.W.M. performed fly husbandry and maintenance. M.A.B. performed larvae behavior experiments and A.W.M. analyzed the data. M.A.B. and K.P. performed confocal experiments and analyzed the data. M.A.B., M.B. and A.W.M. performed electrophysiological experiments and M.A.B. and A.W.M. analyzed the data. M.A.B. and A.M.W wrote the paper with input from A.W.M..

Competing Interests

All authors declare no conflicting financial and non-financial interest.

References

Andlauer TF, Sigrist SJ (2012) Quantitative analysis of Drosophila larval neuromuscular junction morphology. *Cold Spring Harbor protocols* 2012: 490-493

Auld VJ, Fetter RD, Broadie K, Goodman CS (1995) Gliotactin, a novel transmembrane protein on peripheral glia, is required to form the blood-nerve barrier in Drosophila. *Cell* 81: 757-767

Babatz F, Naffin E, Klambt C (2018) The Drosophila Blood-Brain Barrier Adapts to Cell Growth by Unfolding of Pre-existing Septate Junctions. *Dev Cell* 47: 697-710 e693

Banerjee S, Bainton RJ, Mayer N, Beckstead R, Bhat MA (2008) Septate junctions are required for ommatidial integrity and blood-eye barrier function in Drosophila. *Dev Biol* 317: 585-599

Baumgartner S, Littleton JT, Broadie K, Bhat MA, Harbecke R, Lengyel JA, Chiquet-Ehrismann R, Prokop A, Bellen HJ (1996) A Drosophila neurexin is required for septate junction and blood-nerve barrier formation and function. *Cell* 87: 1059-1068

Bittern J, Pogodalla N, Ohm H, Bruser L, Kottmeier R, Schirmeier S, Klambt C (2020) Neuron-glia interaction in the Drosophila nervous system. *Dev Neurobiol*

Bleck TP (1989) Clinical aspects of tetanus. In: *Botulinum neurotoxins and tetanus toxin*, Simpson L.L. (ed.) pp. 379–398. Academic Press: San Diego

Blum FC, Chen C, Kroken AR, Barbieri JT (2012) Tetanus toxin and botulinum toxin a utilize unique mechanisms to enter neurons of the central nervous system. *Infect Immun* 80: 1662-1669

Blum FC, Tepp WH, Johnson EA, Barbieri JT (2014) Multiple domains of tetanus toxin direct entry into primary neurons. *Traffic* 15: 1057-1065

Bomba-Warczak E, Vevea JD, Brittain JM, Figueroa-Bernier A, Tepp WH, Johnson EA, Yeh FL, Chapman ER (2016) Interneuronal Transfer and Distal Action of Tetanus Toxin and Botulinum Neurotoxins A and D in Central Neurons. *Cell Rep* 16: 1974-1987

Brink D, Gilbert M, Auld V (2009) Visualizing the live Drosophila glial-neuromuscular junction with fluorescent dyes. *J Vis Exp*

Bruns D, Engers S, Yang C, Ossig R, Jeromin A, Jahn R (1997) Inhibition of transmitter release correlates with the proteolytic activity of tetanus toxin and botulinus toxin A in individual cultured synapses of Hirudo medicinalis. *The Journal of neuroscience : the official journal of the Society for Neuroscience* 17: 1898-1910

Bruns D, Jahn R (2002) Molecular determinants of exocytosis. *Pflugers Arch* 443: 333-338

Bundgaard M, Abbott NJ (1992) Fine structure of the blood-brain interface in the cuttlefish Sepia officinalis (Mollusca, Cephalopoda). *J Neurocytol* 21: 260-275

Bundgaard M, Abbott NJ (2008) All vertebrates started out with a glial blood-brain barrier 4-500 million years ago. *Glia* 56: 699-708

Carle S, Pirazzini M, Rossetto O, Barth H, Montecucco C (2017) High Conservation of Tetanus and Botulinum Neurotoxins Cleavage Sites on Human SNARE Proteins Suggests That These Pathogens Exerted Little or No Evolutionary Pressure on Humans. *Toxins (Basel)* 9

Carlsen EM, Perrier JF (2014) Purines released from astrocytes inhibit excitatory synaptic transmission in the ventral horn of the spinal cord. *Front Neural Circuits* 8: 60

Carlson SD, Juang JL, Hilgers SL, Garment MB (2000) Blood barriers of the insect. *Annu Rev Entomol* 45: 151-174

Chin AC, Burgess RW, Wong BR, Schwarz TL, Scheller RH (1993) Differential expression of transcripts from syb, a Drosophila melanogaster gene encoding VAMP (synaptobrevin) that is abundant in non-neuronal cells. *Gene* 131: 175-181

Christensen RK, Delgado-Lezama R, Russo RE, Lind BL, Alcocer EL, Rath MF, Fabbiani G, Schmitt N, Lauritzen M, Petersen AV *et al* (2018) Spinal dorsal horn astrocytes release GABA in response to synaptic activation. *J Physiol* 596: 4983-4994

Christensen RK, Petersen AV, Perrier JF (2013) How do glial cells contribute to motor control? *Curr Pharm Des* 19: 4385-4399

Deinhardt K, Berninghausen O, Willison HJ, Hopkins CR, Schiavo G (2006) Tetanus toxin is internalized by a sequential clathrin-dependent mechanism initiated within lipid microdomains and independent of epsin1. *J Cell Biol* 174: 459-471

Deinhardt K, Schiavo G (2005) Endocytosis and retrograde axonal traffic in motor neurons. *Biochem Soc Symp*: 139-150

Deitcher DL, Ueda A, Stewart BA, Burgess RW, Kidokoro Y, Schwarz TL (1998) Distinct requirements for evoked and spontaneous release of neurotransmitter are revealed by mutations in the Drosophila gene neuronal-synaptobrevin. *The Journal of neuroscience : the official journal of the Society for Neuroscience* 18: 2028-2039

DiAntonio A, Burgess RW, Chin AC, Deitcher DL, Scheller RH, Schwarz TL (1993) Identification and characterization of Drosophila genes for synaptic vesicle proteins. *The Journal of neuroscience : the official journal of the Society for Neuroscience* 13: 4924-4935

Edenfeld G, Volohonsky G, Krukkert K, Naffin E, Lammel U, Grimm A, Engelen D, Reuveny A, Volk T, Klambt C (2006) The splicing factor crooked neck associates with the RNA-binding protein HOW to control glial cell maturation in Drosophila. *Neuron* 52: 969-980

Edgar JM, McLaughlin M, Werner HB, McCulloch MC, Barrie JA, Brown A, Faichney AB, Snaidero N, Nave KA, Griffiths IR (2009) Early ultrastructural defects of axons and axon-glia junctions in mice lacking expression of Cnp1. *Glia* 57: 1815-1824

Edgar JM, McLaughlin M, Yool D, Zhang SC, Fowler JH, Montague P, Barrie JA, McCulloch MC, Duncan ID, Garbern J *et al* (2004) Oligodendroglial modulation of fast axonal transport in a mouse model of hereditary spastic paraplegia. *J Cell Biol* 166: 121-131

Elferink LA, Trimble WS, Scheller RH (1989) Two vesicle-associated membrane protein genes are differentially expressed in the rat central nervous system. *J Biol Chem* 264: 11061-11064

Erdmann G, Wiegand H, Wellhoner HH (1975) Intraaxonal and extraaxonal transport of 125I-tetanus toxin in early local tetanus. *Naunyn Schmiedebergs Arch Pharmacol* 290: 357-373

Fields RD (2015) A new mechanism of nervous system plasticity: activity-dependent myelination. *Nat Rev Neurosci* 16: 756-767

Fuentes-Medel Y, Logan MA, Ashley J, Ataman B, Budnik V, Freeman MR (2009) Glia and muscle sculpt neuromuscular arbors by engulfing destabilized synaptic boutons and shed presynaptic debris. *PLoS Biol* 7: e1000184

Funfschilling U, Supplie LM, Mahad D, Boretius S, Saab AS, Edgar J, Brinkmann BG, Kassmann CM, Tzvetanova ID, Mobius W *et al* (2012) Glycolytic oligodendrocytes maintain myelin and long-term axonal integrity. *Nature* 485: 517-521

Griffiths I, Klugmann M, Anderson T, Yool D, Thomson C, Schwab MH, Schneider A, Zimmermann F, McCulloch M, Nadon N *et al* (1998) Axonal swellings and degeneration in mice lacking the major proteolipid of myelin. *Science* 280: 1610-1613

Gucek A, Vardjan N, Zorec R (2012) Exocytosis in astrocytes: transmitter release and membrane signal regulation. *Neurochem Res* 37: 2351-2363

Halestrap AP, Wilson MC (2012) The monocarboxylate transporter family--role and regulation. *IUBMB Life* 64: 109-119

Hardiman O, Al-Chalabi A, Chio A, Corr EM, Logroscino G, Robberecht W, Shaw PJ, Simmons Z, van den Berg LH (2017) Amyotrophic lateral sclerosis. *Nat Rev Dis Primers* 3: 17085

Hoogstraaten RI, van Keimpema L, Toonen RF, Verhage M (2020) Tetanus insensitive VAMP2 differentially restores synaptic and dense core vesicle fusion in tetanus neurotoxin treated neurons. *Sci Rep* 10: 10913

Huba R, Hofmann HD (1988) Tetanus toxin binding to isolated and cultured rat retinal glial cells. *Glia* 1: 156-164

Jahn R, Fasshauer D (2012) Molecular machines governing exocytosis of synaptic vesicles. *Nature* 490: 201-207

Jahn R, Scheller RH (2006) SNAREs--engines for membrane fusion. *Nat Rev Mol Cell Biol* 7: 631-643

Kerr KS, Fuentes-Medel Y, Brewer C, Barria R, Ashley J, Abruzzi KC, Sheehan A, Tasdemir-Yilmaz OE, Freeman MR, Budnik V (2014) Glial wingless/Wnt regulates glutamate receptor clustering and synaptic physiology at the Drosophila neuromuscular junction. *The Journal of neuroscience : the official journal of the Society for Neuroscience* 34: 2910-2920

Kuo IY, Ehrlich BE (2015) Signaling in muscle contraction. *Cold Spring Harb Perspect Biol* 7: a006023

Lalli G, Gschmeissner S, Schiavo G (2003) Myosin Va and microtubule-based motors are required for fast axonal retrograde transport of tetanus toxin in motor neurons. *J Cell Sci* 116: 4639-4650

Lee HS, Ghetti A, Pinto-Duarte A, Wang X, Dziewczapolski G, Galimi F, Huitron-Resendiz S, Pina-Crespo JC, Roberts AJ, Verma IM *et al* (2014) Astrocytes contribute to gamma oscillations and recognition memory. *Proceedings of the National Academy of Sciences of the United States of America* 111: E3343-3352

Lee T, Luo L (1999) Mosaic analysis with a repressible cell marker for studies of gene function in neuronal morphogenesis. *Neuron* 22: 451-461

Lee Y, Morrison BM, Li Y, Lengacher S, Farah MH, Hoffman PN, Liu Y, Tsingalia A, Jin L, Zhang PW *et al* (2012) Oligodendroglia metabolically support axons and contribute to neurodegeneration. *Nature* 487: 443-448

Leiserson WM, Harkins EW, Keshishian H (2000) Fray, a Drosophila serine/threonine kinase homologous to mammalian PASK, is required for axonal ensheathment. *Neuron* 28: 793-806

Li H, Russo A, DiAntonio A (2019) SIK3 suppresses neuronal hyperexcitability by regulating the glial capacity to buffer K(+) and water. *J Cell Biol* 218: 4017-4029

Liu L, MacKenzie KR, Putluri N, Maletic-Savatic M, Bellen HJ (2017) The Glia-Neuron Lactate Shuttle and Elevated ROS Promote Lipid Synthesis in Neurons and Lipid Droplet Accumulation in Glia via APOE/D. *Cell Metab* 26: 719-737 e716

Machler P, Wyss MT, Elsayed M, Stobart J, Gutierrez R, von Faber-Castell A, Kaelin V, Zuend M, San Martin A, Romero-Gomez I *et al* (2016) In Vivo Evidence for a Lactate Gradient from Astrocytes to Neurons. *Cell Metab* 23: 94-102

McMahon HT, Ushkaryov YA, Edelmann L, Link E, Binz T, Niemann H, Jahn R, Sudhof TC (1993) Cellubrevin is a ubiquitous tetanus-toxin substrate homologous to a putative synaptic vesicle fusion protein. *Nature* 364: 346-349

Nakai M, Chen L, Nowak RA (2006) Tissue distribution of basigin and monocarboxylate transporter 1 in the adult male mouse: a study using the wild-type and basigin gene knockout mice. *Anat Rec A Discov Mol Cell Evol Biol* 288: 527-535

Nave KA (2010) Myelination and the trophic support of long axons. *Nat Rev Neurosci* 11: 275-283

Oshima K, Fehon RG (2011) Analysis of protein dynamics within the septate junction reveals a highly stable core protein complex that does not include the basolateral polarity protein Discs large. *J Cell Sci* 124: 2861-2871

Pascual O, Casper KB, Kubera C, Zhang J, Revilla-Sanchez R, Sul JY, Takano H, Moss SJ, McCarthy K, Haydon PG (2005) Astrocytic purinergic signaling coordinates synaptic networks. *Science* 310: 113-116

Patarnello T, Bargelloni L, Rossetto O, Schiavo G, Montecucco C (1993) Neurotransmission and secretion. *Nature* 364: 581-582

Perea G, Araque A (2007) Astrocytes potentiate transmitter release at single hippocampal synapses. *Science* 317: 1083-1086

Petersen SA, Fetter RD, Noordermeer JN, Goodman CS, DiAntonio A (1997) Genetic analysis of glutamate receptors in Drosophila reveals a retrograde signal regulating presynaptic transmitter release. *Neuron* 19: 1237-1248

Pierre K, Pellerin L (2005) Monocarboxylate transporters in the central nervous system: distribution, regulation and function. *J Neurochem* 94: 1-14

Popoff MR, Poulain B (2010) Bacterial toxins and the nervous system: neurotoxins and multipotential toxins interacting with neuronal cells. *Toxins (Basel)* 2: 683-737

Qin G, Schwarz T, Kittel RJ, Schmid A, Rasse TM, Kappei D, Ponimaskin E, Heckmann M, Sigrist SJ (2005) Four different subunits are essential for expressing the synaptic glutamate receptor at neuromuscular junctions of Drosophila. *The Journal of neuroscience : the official journal of the Society for Neuroscience* 25: 3209-3218

Rao S, Lang C, Levitan ES, Deitcher DL (2001) Visualization of neuropeptide expression, transport, and exocytosis in Drosophila melanogaster. *J Neurobiol* 49: 159-172

Rummel A (2017) Two Feet on the Membrane: Uptake of Clostridial Neurotoxins. In: *Uptake and Trafficking of Protein Toxins*, Barth H. (ed.) pp. 1-37. Springer International Publishing: Cham

Schiavo G, Benfenati F, Poulain B, Rossetto O, Polverino de Laureto P, DasGupta BR, Montecucco C (1992) Tetanus and botulinum-B neurotoxins block neurotransmitter release by proteolytic cleavage of synaptobrevin. *Nature* 359: 832-835

Schiavo G, Matteoli M, Montecucco C (2000) Neurotoxins affecting neuroexocytosis. *Physiol Rev* 80: 717-766

Schuster CM, Ultsch A, Schloss P, Cox JA, Schmitt B, Betz H (1991) Molecular cloning of an invertebrate glutamate receptor subunit expressed in Drosophila muscle. *Science* 254: 112-114

Schwab ME, Thoenen H (1976) Electron microscopic evidence for a transsynaptic migration of tetanus toxin in spinal cord motoneurons: an autoradiographic and morphometric study. *Brain Res* 105: 213-227

Schwab ME, Thoenen H (1978) Selective binding, uptake, and retrograde transport of tetanus toxin by nerve terminals in the rat iris. An electron microscope study using colloidal gold as a tracer. *J Cell Biol* 77: 1-13

Schwabe T, Bainton RJ, Fetter RD, Heberlein U, Gaul U (2005) GPCR signaling is required for blood-brain barrier formation in drosophila. *Cell* 123: 133-144

Schwarz Y, Zhao N, Kirchhoff F, Bruns D (2017) Astrocytes control synaptic strength by two distinct v-SNARE-dependent release pathways. *Nat Neurosci* 20: 1529-1539

Sepp KJ, Auld VJ (1999) Conversion of lacZ enhancer trap lines to GAL4 lines using targeted transposition in Drosophila melanogaster. *Genetics* 151: 1093-1101

Sepp KJ, Schulte J, Auld VJ (2001) Peripheral glia direct axon guidance across the CNS/PNS transition zone. *Dev Biol* 238: 47-63

Sievers F, Wilm A, Dineen D, Gibson TJ, Karplus K, Li W, Lopez R, McWilliam H, Remmert M, Soding J *et al* (2011) Fast, scalable generation of high-quality protein multiple sequence alignments using Clustal Omega. *Mol Syst Biol* 7: 539

Sigrist SJ, Reiff DF, Thiel PR, Steinert JR, Schuster CM (2003) Experience-dependent strengthening of Drosophila neuromuscular junctions. *The Journal of neuroscience : the official journal of the Society for Neuroscience* 23: 6546-6556

Simard M, Nedergaard M (2004) The neurobiology of glia in the context of water and ion homeostasis. *Neuroscience* 129: 877-896

Stewart BA, Atwood HL, Renger JJ, Wang J, Wu CF (1994) Improved stability of Drosophila larval neuromuscular preparations in haemolymph-like physiological solutions. *Journal of comparative physiology A, Sensory, neural, and behavioral physiology* 175: 179-191

Stork T, Engelen D, Krudewig A, Silies M, Bainton RJ, Klambt C (2008) Organization and function of the blood-brain barrier in Drosophila. *The Journal of neuroscience : the official journal of the Society for Neuroscience* 28: 587-597

Sudhof TC, Baumert M, Perin MS, Jahn R (1989) A synaptic vesicle membrane protein is conserved from mammals to Drosophila. *Neuron* 2: 1475-1481

Sun B, Xu P, Salvaterra PM (1999) Dynamic visualization of nervous system in live Drosophila. *Proceedings of the National Academy of Sciences of the United States of America* 96: 10438-10443

Surana S, Tosolini AP, Meyer IFG, Fellows AD, Novoselov SS, Schiavo G (2018) The travel diaries of tetanus and botulinum neurotoxins. *Toxicon* 147: 58-67

Sweeney ST, Broadie K, Keane J, Niemann H, O'Kane CJ (1995) Targeted expression of tetanus toxin light chain in Drosophila specifically eliminates synaptic transmission and causes behavioral defects. *Neuron* 14: 341-351

Szigeti K, Lupski JR (2009) Charcot-Marie-Tooth disease. *Eur J Hum Genet* 17: 703-710

Tiklova K, Senti KA, Wang S, Graslund A, Samakovlis C (2010) Epithelial septate junction assembly relies on melanotransferrin iron binding and endocytosis in Drosophila. *Nat Cell Biol* 12: 1071-1077

Ullrich A, Bohme MA, Schoneberg J, Depner H, Sigrist SJ, Noe F (2015) Dynamical Organization of Syntaxin-1A at the Presynaptic Active Zone. *PLoS computational biology* 11: e1004407

Willison HJ, Jacobs BC, van Doorn PA (2016) Guillain-Barre syndrome. *Lancet* 388: 717-727

Yeh FL, Dong M, Yao J, Tepp WH, Lin G, Johnson EA, Chapman ER (2010) SV2 mediates entry of tetanus neurotoxin into central neurons. *PLoS Pathog* 6: e1001207

Yildirim K, Petri J, Kottmeier R, Klambt C (2019) Drosophila glia: Few cell types and many conserved functions. *Glia* 67: 5-26

Zhang B, Stewart B (2010) Electrophysiological recording from Drosophila larval body-wall muscles. *Cold Spring Harb Protoc* 2010: pdb prot5487

Zuchero JB, Barres BA (2015) Glia in mammalian development and disease. *Development* 142: 3805-3809

Figure legends

Figure 1: Pan-glial TeNT-LC expression causes paralysis, disrupts nerve integrity, and results in motoneural hyperactivity. A,B Sketches of dissected larvae depicting segmental nerves radiating from the brain (A) containing muscle innervating, glia ensheathed motoneurons (B, left; nerve cross section, right, according to (Stork *et al.*, 2008)). **C,D** Analysis of larval movement with example tracks over 85s (C), distances travelled over time (85s; D, left) and comparison of final distances travelled by 3rd instar larvae of the indicated genotypes (D, right): *Repo::+* (black), *TeNT-LC::+* (grey) and *Repo::TeNT-LC* (red). See also Videos 1-3**. E,F** Nerves of segments A2–A4 (E) and quantification of axonal area, nerve morphology and BRP spots per nerve (F) were investigated in the region of interest (ROI) illustrated in panel A in 3rd-instar larvae of *Repo::+* (black), *TeNT-LC::+* (grey) and *Repo::TeNT-LC* (red) animals. Dashed line in (E, BRP) indicates nerve area and arrow head indicates defasciculated single axon. **G,H** Representative mEPSP (spont.) and eEPSP (evoked) traces (G) and quantification of mEPSP/eEPSP amplitudes, % of recorded cells displaying normal activity (single eEPSP in response to single stimulation) and the number of response peaks per stimuli in *Repo::+* (black), *TeNT-LC::+* (grey) and *Repo::TeNT-LC* (red) animals. Asterisks indicate postsynaptic response peaks (eEPSP). Scale bars: (C) 1 cm; (E) 10 µm; (G) mEPSP: 1 s, 2 mV. eEPSP: 25 ms, 5 mV. Statistics: nonparametric one-way analysis of variance (ANOVA) test, followed by Tukey's multiple comparison test except for (F, nerve morphology) where a nonparametric Kruskal-Wallis test was performed. ***$p \leq 0.001$; **$p \leq 0.01$; *$p \leq 0.05$; n.s. (not significant) $p > 0.05$. (C,D) *Repo::+:* six larvae; *TeNT::+:* nine larvae; *Repo::TeNT:* 11 larvae; (E,F) *Repo::+:* 17 nerves, six larvae; *TeNT::+:* 18 nerves, six larvae; *Repo::TeNT:* 18 nerves, six larvae; (G,H) *Repo::+:* 8 cells, four larvae; *TeNT::+:* 7 cells, four larvae; *Repo::TeNT:* 8 cells, four larvae. All panels show mean ± s.e.m.

Figure 2: Syb but not nSyb is targeted by TeNT-LC in glial cells. A Sketch of a membrane docked vesicle depicting the SNARE proteins and the v-SNARE attack point of TeNT-LC. **B** Sequence alignment of Isoforms A of *Drosophila* nSyb (magenta) and Syb (blue). SNARE motif (yellow shaded) and the TeNT-LC cleavage site (QF, red box) are highlighted. Alignment performed using Clustal Omega. Gonnet PAM250 matrix used to compare sequence substitutions: * identical aa, : score >0.5, . score <0.5, "gap" score below 0. **C-F** Nerves of segments A2–A4 (C,E) and quantification of axonal area, nerve morphology and BRP spots per nerve (D,F) from 3rd-instar larvae of the indicated genotypes. Dashed line in C,E indicates nerve area. **G,H** Representative mEPSP (spont.) and eEPSP (evoked) traces (G) and quantification of mEPSP/eEPSP amplitudes, % of recorded cells displaying normal activity (single eEPSP in response to single stimulation) and the normalized number of response peaks per stimulus in *Repo::+* (black), *Syb-RNAi::+* (grey) and *Repo::Syb-RNAi* (red) animals. Asterisks indicate postsynaptic response peaks (eEPSP). Scale bars: (C, E) 10 µm (G) mEPSP: 1 s, 2 mV. eEPSP: 25 ms, 5 mV. Statistics: nonparametric one-way analysis of variance (ANOVA) test, followed by Tukey's multiple comparison test except for (D, F: nerve morphology) where a nonparametric Kruskal-Wallis test was performed. ***$p \leq 0.001$; *$p \leq 0.05$; n.s. (not significant) $p > 0.05$. (C,D) *Repo::+:* 15 nerves, six larvae; *nSyb-RNAi::+:* 15 nerves, six larvae; *Repo::nSyb-RNAi:* 15 nerves, six larvae; (E,F) *Repo::+:* 19 nerves, six larvae; *Syb-RNAi::+:* 18 nerves, six larvae; *Repo::Syb-RNAi:* 19 nerves, six larvae; (G,H) *Repo::+:* 9 cells, five larvae; *Syb-RNAi::+:* 10 cells, five larvae; *Repo::Syb-RNAi: 10* cells, five larvae. All panels show mean ± s.e.m.

Figure 3: TeNT-LC action in SPGs disrupts axonal transport, causes nerve disintegration, hyperactivity and impairs SJ formation. A Cross section sketch of glial ensheathed motoneuron axon highlighting SPGs (purple). Red circle highlights septate junction (SJ). **B,C** Examples of muscle 4 NMJs of segments A2–A4 from 3rd-instar larvae expressing CD8-GFP in SPGs (left) with (left & bottom) and without (right top) SPG ensheathment of the NMJ. **C** Quantification of % of NMJs with/without SPG ensheatment. **D,E** Nerves of segments A2–A4 (D) and quantification of axonal area, nerve morphology and BRP spots per nerve (E) from 3rd-instar larvae of *rL82::+* (black), *TeNT-LC::+* (grey) and *rL82::TeNT-LC* (red) animals. Dashed line in D indicates nerve area. **F,G** Representative mEPSP (spont.) and eEPSP (evoked) traces (F; for rl82::TeNT-LC a one normal and one hyperactive trace is shown) and quantification of mEPSP/eEPSP amplitudes, % of recorded cells displaying normal activity (single eEPSP in response to single stimulation) and the normalized number of response peaks per stimulus in *rL82::+* (black), *TeNT-LC::+* (grey) and *rL82::TeNT-LC* (red) animals (G). Asterisks indicate postsynaptic response peaks (eEPSP). **H-J** Nerves of segments A2–A4 (H), vertical line profiles across nerve NrxIV-GFP signals (I; solid line GFP signal, dashed line HRP signal) and orthogonal nerve cross section (J) from 3rd-instar larvae of *rL82::NrxIV-GFP* and *rL82::NrxIV-GFP::TeNT* (two examples are shown). Lines in H indicate line profile positions shown in I. **K-N** Same as in D-G but for *rL82::+* (black), *NrxIV-RNAi::+* (grey) and *rL82::NrxIV-RNAi* (red) animals. Scale bars: (B) 5 µm; (D,H,K) 10 µm; (J) 2.5 µm; (F) mEPSP: 1 s, 2 mV; eEPSP: 25 ms, 5 mV. Statistics: nonparametric one-way analysis of variance (ANOVA) test, followed by Tukey's multiple comparison test except for (E; L: nerve morphology) where a nonparametric Kruskal-Wallis test was performed. ***$p \leq 0.001$; **$p \leq 0.01$; *$p \leq 0.05$; n.s. (not significant) $p > 0.05$. (B,C) 26 NMJs, seven larvae; (D,E) *rL82::+:* 18 nerves, six larvae; *TeNT::+:* 17 nerves, four larvae; *rL82::TeNT:* 20 nerves, six larvae; (F,G) *rL82::+:* 10 cells, five larvae; *TeNT::+:* 10 cells, five larvae; *rL82::TeNT:* 10 cells, five larvae; (H-J) *rL82::NrxIV-GFP:* 18 nerves, six

larvae; *rL82::NrxIV-GFP::TeNT:* 18 nerves, six larvae; (K,L) *rL82::+:* 17 nerves, six larvae; *NrxIV-RNAi::+:* 17 nerves, six larvae; *rL82::NrxIV-GFP:* 18 nerves, six larvae; (M,N) *rL82::+:* 12 cells, seven larvae; *NrxIV-RNAi::+:* 13 cells, seven larvae; *rL82::NrxIV-GFP:* 14 cells, seven larvae. All panels show mean ± s.e.m.

Figure 4: TeNT-LC action in WGs causes axonal BRP accumulation similarly to Basigin-KD. A Cross section sketch of glial ensheathed motoneuron axon highlighting WGs (brown). **B,C** Example of muscle 4 NMJs of segments A2–A4 from 3rd-instar larvae expressing CD8-GFP in WGs (left) with enhanced GFP laser intensity (right). **C** Quantification of % of NMJs with/without WG ensheatment. **D,E** Nerves of segments A2–A4 (D) and quantification of axonal area, nerve morphology and BRP spots per nerve (E) from 3rd-instar larvae of *Nrv2::+* (black), *TeNT-LC::+* (grey) and *Nrv2::TeNT-LC* (red) animals. Dashed line in D indicates nerve area. **F,G** Same as in D,E but for *Nrv2::+* (black), *Basigin-RNAi::+* (grey) and *Nrv2::Basigin-RNAi* (red) animals. Scale bars: (B) 5 µm; (D,F) 10 µm. Statistics: nonparametric one-way analysis of variance (ANOVA) test, followed by Tukey's multiple comparison test except for (E; G: nerve morphology) where a nonparametric Kruskal-Wallis test was performed. ***$p \leq 0.001$; n.s. (not significant) $p > 0.05$. (B,C) 23 NMJs, six larvae; (D, E) *Nrv2::+*: 17 nerves, six larvae; *TeNT::+:* 17 nerves, six larvae; *Nrv2::TeNT*: 18 nerves, six larvae; (F,G) *Nrv2::+*: 17 nerves, six larvae; *Basigin-RNAi::+:* 17 nerves, five larvae; *Nrv2::Basigin-RNAi*: 18 nerves, six larvae. All panels show mean ± s.e.m.

Expanded view figure legends

Expanded view figure 1 (Fig. EV1): TeNT-LC expression in SPGs impairs larval movement but does not kill SPG cells. A,B Analysis of larval movement with example tracks over 85s (A), distances travelled over time (85s; B, left) and comparison of final distances travelled by larvae of the indicated genotypes (B, right). See also Videos 4, 2, 5. TeNT-LC data (Video 2) was replotted from Fig. 1C,D. **C,D** Nerves of segments A2–A4 (C) and quantification of GFP intensity per nerve area (D) from 3rd-instar larvae of *rL82::CD8-GFP* (black) and *rL82::CD8-GFP::TeNT-LC* (red) animals. **E,F** same as in C,D but for *rL82::syb-RNAi* (black) and *rL82::CD8-GFP::Syb-RNAi* (red) animals. Scale bars: (A) 1 cm; (C,E) 10 µm. Statistics: nonparametric one-way analysis of variance (ANOVA) test, followed by Tukey's multiple comparison test (A), Student's t test (B) and Mann-Whitney U test (C). ***$p \leq 0.001$; **$p \leq 0.01$; *$p \leq 0.05$; n.s. (not significant) $p > 0.05$. (A,B) *rL82::+:* nine larvae; *TeNT::+:* nine larvae; *rL82::TeNT:* 11 larvae; (C,D) *rl82::CD8-GFP*: 17 nerves, six larvae; *rl82::CD8-GFP::TeNT*: 18 nerves, six larvae; (E,F) *rl82::CD8-GFP*: 19 nerves, six larvae; *rl82::CD8-GFP::Syb-RNAi*: 18 nerves, six larvae. All panels show mean ± s.e.m.

Expanded view figure 2 (Fig. EV2). Syb is targeted by TeNT-LC in SPGs. A,B Nerves of segments A2–A4 (A; neural lamella visualized via GluRIID staining), orthogonal nerve cross section (B) and quantification of BRP spots per nerve, axonal BRP spot area, axonal/lamella area and nerve morphology (C) from 3rd-instar larvae of *rL82::+* (black), *Syb-RNAi::+* (grey) and *rL82:: Syb-RNAi* (red) animals. **D,E** Representative mEPSP (spont.) and eEPSP (evoked) traces (D) and quantification of mEPSP/eEPSP amplitudes, % of recorded cells displaying normal activity and the normalized number of response peaks per stimulus (E) of *rL82::+* (black), *Syb-RNAi::+* (grey) and *rL82:: Syb-RNAi* (red) animals (G). Asterisks indicate postsynaptic response peaks (eEPSP). **F,G** Nerves of segments A2–A4 (F) and quantification of axonal area, nerve morphology and BRP spots per nerve (G) from 3rd-instar larvae of *rL82::+* (black), *nSyb-RNAi::+* (grey) and *rL82::nSyb-RNAi* (red) animals. Dashed lines indicate nerve areas. **H,I** Nerves of segments A2–A4 (H) and quantification of ANF spots per nerve (I) from 3rd-instar larvae of *rL82::ANF-EMD* (black) and *rL82::ANF-EMD::TeNT* (red) animals. Scale bars: (A, F, H) 10 µm; (B) 2.5µm; (D) mEPSP: 1 s, 2 mV; eEPSP: 25 ms, 5 mV. Statistics: nonparametric one-way analysis of variance (ANOVA) test, followed by Tukey's multiple comparison test except for (C,G: nerve morphology) where a nonparametric Kruskal-Wallis test and (I) where a Student's t test was performed. ***$p \leq 0.001$; **$p \leq 0.01$; *$p \leq 0.05$; n.s. (not significant) $p > 0.05$. (A-C) *rl82::+*: 18 nerves, six larvae; *Syb-RNAi::+*: 17 nerves, six larvae; *rL82::Syb-RNAi*: 20 nerves, six larvae; (D,E) *rl82::+*: 10 cells, five larvae; *Syb-RNAi::+*: 10 cells, five larvae; *rL82::Syb-RNAi*: 10 cells, five larvae; (F,G) *rl82::+*: 15 nerves, five larvae; *nSyb-RNAi::+*: 18 nerves, six larvae; *rL82::nSyb-RNAi*: 18 nerves, six larvae; (H,I) *rL82::ANF-EMD*: 19 nerves, six larvae; *rL82::ANF-EMD::Syb-RNAi*: 18 nerves, six larvae. All panels show mean ± s.e.m.

Expanded view figure 3 (Fig. EV3). WGs support axonal transport. A,B Nerves of segments A2–A4 (A) and quantification of GFP intensity per nerve area (B) from 3rd-instar larvae of *Nrv2::CD8-GFP* (black) and *Nrv2::CD8-GFP::TeNT-LC* (red) animals. **C-E** Nerves of segments A2–A4 (C; neural lamella visualized via GluRIID staining), orthogonal nerve cross section (D) and quantification of axonal/lamella area (E) from 3rd-instar larvae of *Nrv2::+* (black), *Basigin-RNAi::+* (grey) and *Nrv2::Basigin-RNAi* (red) animals. **F-G** Nerves of segments A2–A4 (F) and quantification of axonal area, nerve morphology and BRP spots per nerve (G) from 3rd-instar larvae of *rL82::+* (black), *Basigin-RNAi::+* (grey) and *rL82::Basigin-RNAi* (red) animals. Scale bars: (A, C, F) 10 µm; (D) 2.5 µm. Statistics: nonparametric one-way analysis of variance (ANOVA) test, followed by Tukey's multiple comparison test except for (G, nerve morphology) where a nonparametric Kruskal-Wallis test was performed and (B) where a Mann-Whitney U Test was performed. ***$p \leq 0.001$; **$p \leq 0.01$; *$p \leq 0.05$; n.s. (not significant) $p > 0.05$. (A,B) *Nrv2::CD8-GFP*: 18 nerves, six larvae; *Nrv2::CD8-GFP::TeNT*: 21 nerves, six larvae; (C-E) *Nrv2::+*: 17 nerves, six larvae; *Basigin-RNAi::+:* 17 nerves, five larvae; *Nrv2::Basigin-RNAi*: 18 nerves, six larvae; (F,G) *rL82::+*: 17 nerves, six larvae; *Basigin-RNAi::+:* 18 nerves, six larvae; *rL82::Basigin-RNAi*: 18 nerves, six larvae. All panels show mean ± s.e.m.

Video legends

Video 1-3: Pan-glial TeNT-LC expression severely impairs larval movement. Video of larval movement over 85s for *Repo::+* (Video 1), *TeNT::+* (Video 2) and *Repo::TeNT* (Video 3). See also Figure 1C,D for analysis**.**

Video 4,5: TeNT-LC expression in SPGs severely impairs larval movement. Video of larval movement over 85s for rL82::+ (Video 4), TeNT::+ (Video 2) and *rL82::TeNT* (Video 5). See also Fig. EV1A,B for analysis**.**

Video 6: TeNT-LC expression in SPGs severely paralyzes adult flies. Video of two *rL82::TeNT-LC-LC* flies and one control. *rL82::TeNT-LC-LC* flies are severely paralyzed (uncoordinated or no movement; inability to turn around when laying on their backs; no reaction to banging) while the control fly rapidly moves upwards after bang-shock.

Figure 1:

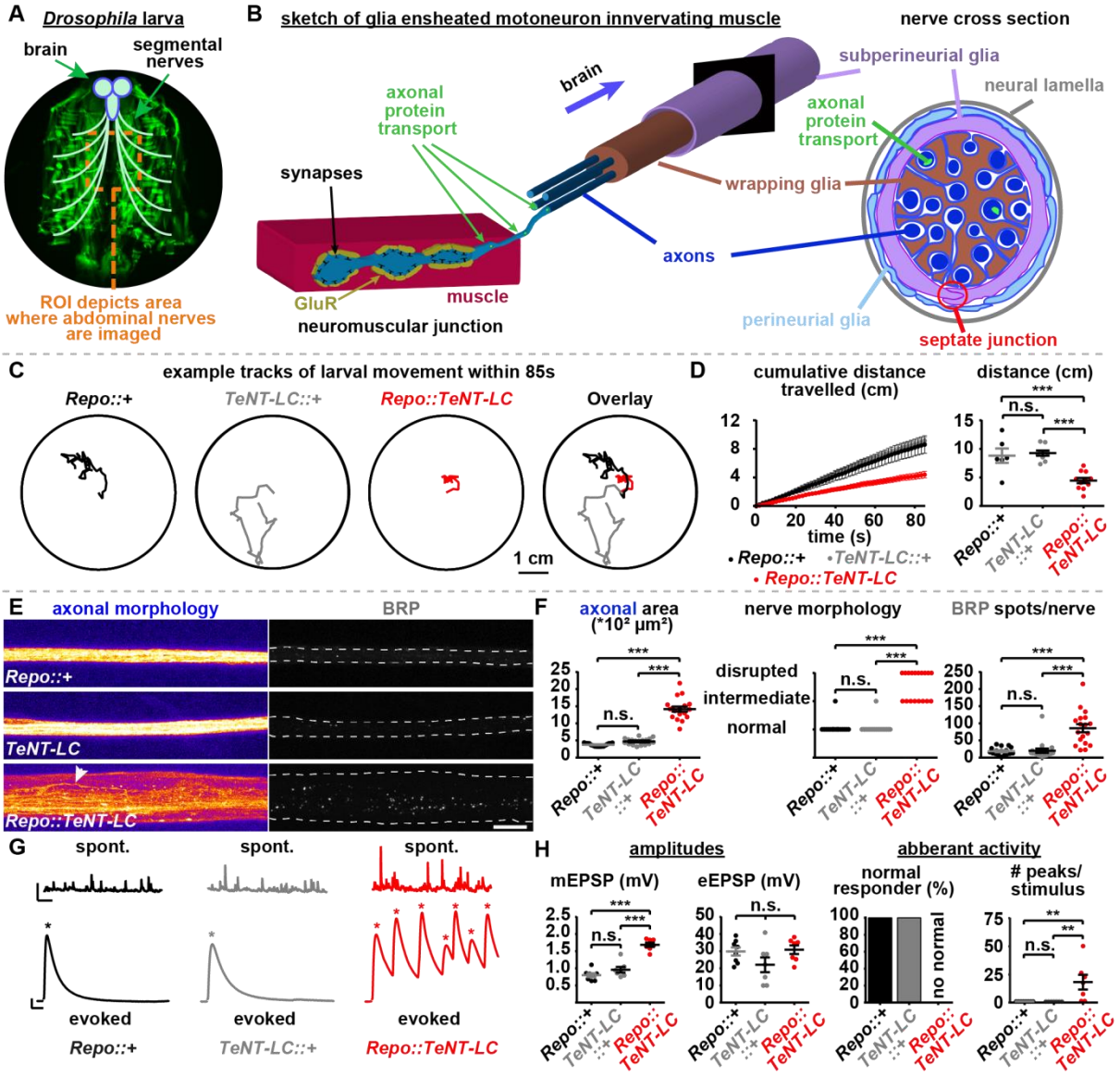

Figure 1: Pan-glial TeNT-LC expression causes paralysis, disrupts nerve integrity, and results in motoneural hyperactivity. A,B Sketches of dissected larvae depicting segmental nerves radiating from the brain (A) containing muscle innervating, glia ensheathed motoneurons (B, left; nerve cross section, right, according to (Stork *et al.*, 2008)). **C,D** Analysis of larval movement with example tracks over 85s (C), distances travelled over time (85s; D, left) and comparison of final distances travelled by 3rd instar larvae of the indicated genotypes (D, right): *Repo::+* (black), *TeNT-LC::+* (grey) and *Repo::TeNT-LC* (red). See also Videos 1-3**. E,F** Nerves of segments A2–A4 (E) and quantification of axonal area, nerve morphology and BRP spots per nerve (F) were investigated in the region of interest (ROI) illustrated in panel A in 3rd-instar larvae of *Repo::+* (black), *TeNT-LC::+* (grey) and *Repo::TeNT-LC* (red) animals. Dashed line in (E, BRP) indicates nerve area and arrow head indicates defasciculated single axon. **G,H** Representative mEPSP (spont.) and eEPSP (evoked) traces (G) and quantification of mEPSP/eEPSP amplitudes, % of recorded cells displaying normal activity (single

eEPSP in response to single stimulation) and the number of response peaks per stimuli in *Repo::+* (black), *TeNT-LC::+* (grey) and *Repo::TeNT-LC* (red) animals. Asterisks indicate postsynaptic response peaks (eEPSP). Scale bars: (C) 1 cm; (E) 10 µm; (G) mEPSP: 1 s, 2 mV. eEPSP: 25 ms, 5 mV. Statistics: nonparametric one-way analysis of variance (ANOVA) test, followed by Tukey's multiple comparison test except for (F, nerve morphology) where a nonparametric Kruskal-Wallis test was performed. ***$p \leq 0.001$; **$p \leq 0.01$; *$p \leq 0.05$; n.s. (not significant) $p > 0.05$. (C,D) *Repo::+:* six larvae; *TeNT::+:* nine larvae; *Repo::TeNT:* 11 larvae; (E,F) *Repo::+:* 17 nerves, six larvae; *TeNT::+:* 18 nerves, six larvae; *Repo::TeNT:* 18 nerves, six larvae; (G,H) *Repo::+:* 8 cells, four larvae; *TeNT::+:* 7 cells, four larvae; *Repo::TeNT:* 8 cells, four larvae. All panels show mean ± s.e.m.

Figure 2:

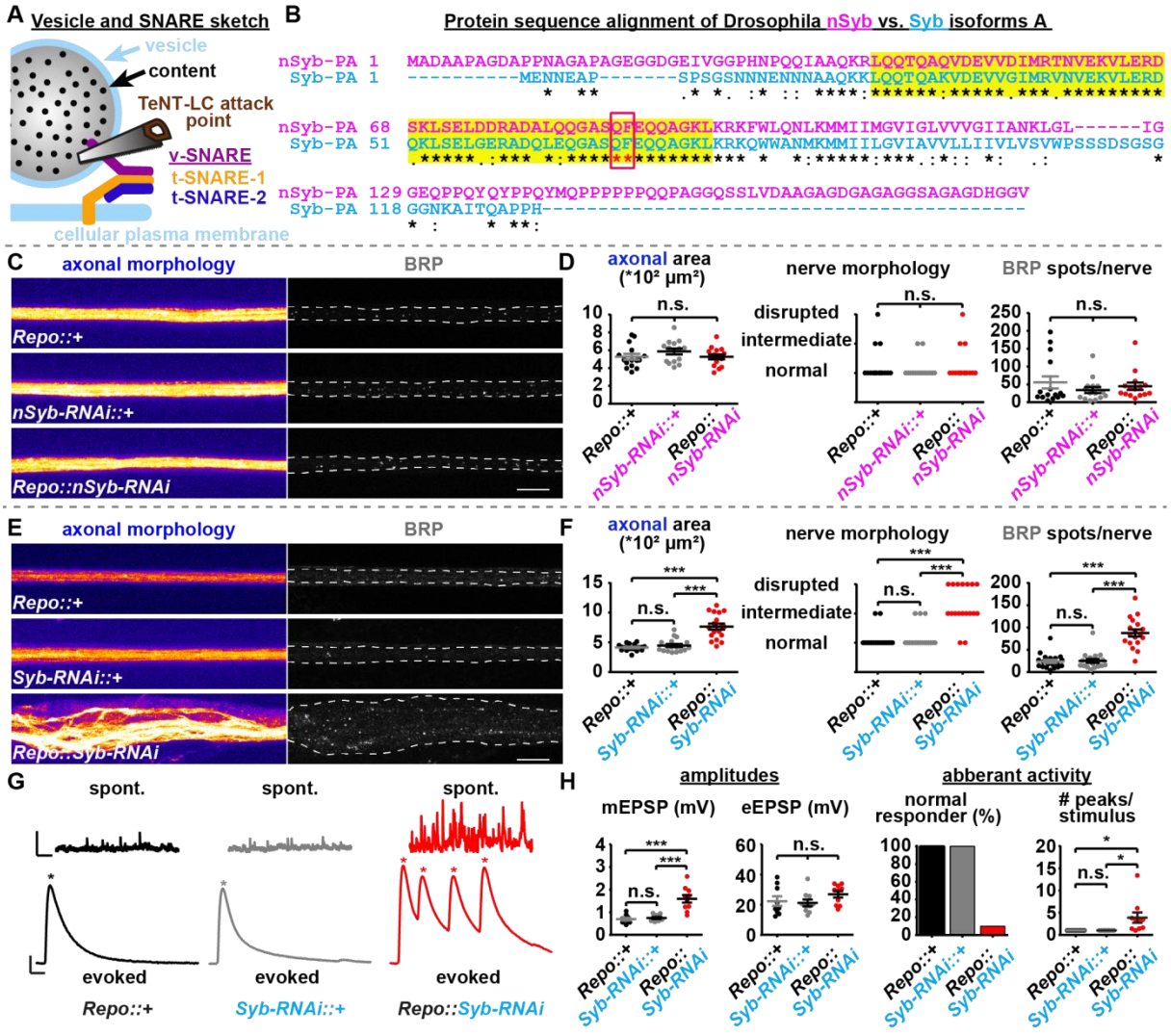

Figure 2: Syb but not nSyb is targeted by TeNT-LC in glial cells. A Sketch of a membrane docked vesicle depicting the SNARE proteins and the v-SNARE attack point of TeNT-LC. **B** Sequence alignment of Isoforms A of *Drosophila* nSyb (magenta) and Syb (blue). SNARE motif (yellow shaded) and the TeNT-LC cleavage site (QF, red box) are highlighted. Alignment performed using Clustal Omega. Gonnet PAM250 matrix used to compare sequence substitutions: * identical aa, : score >0.5, . score <0.5, "gap" score below 0. **C-F** Nerves of segments A2–A4 (C,E) and quantification of axonal area, nerve morphology and BRP spots per nerve (D,F) from 3rd-instar larvae of the indicated genotypes. Dashed line in C,E indicates nerve area. **G,H** Representative mEPSP (spont.) and eEPSP (evoked) traces (G) and quantification of mEPSP/eEPSP amplitudes, % of recorded cells displaying normal activity (single eEPSP in response to single stimulation) and the normalized number of response peaks per stimulus in *Repo::+* (black), *Syb-RNAi::+* (grey) and *Repo::Syb-RNAi* (red) animals. Asterisks indicate postsynaptic response peaks (eEPSP). Scale bars: (C, E) 10 µm (G) mEPSP: 1 s, 2 mV. eEPSP: 25 ms, 5 mV. Statistics: nonparametric one-way analysis of variance (ANOVA) test, followed by Tukey's multiple comparison test except for (D, F: nerve morphology)

where a nonparametric Kruskal-Wallis test was performed. ***$p \leq 0.001$; *$p \leq 0.05$; n.s. (not significant) $p > 0.05$. (C,D) *Repo::+:* 15 nerves, six larvae; *nSyb-RNAi::+:* 15 nerves, six larvae; *Repo::nSyb-RNAi:* 15 nerves, six larvae; (E,F) *Repo::+:* 19 nerves, six larvae; *Syb-RNAi::+:* 18 nerves, six larvae; *Repo::Syb-RNAi:* 19 nerves, six larvae; (G,H) *Repo::+:* 9 cells, five larvae; *Syb-RNAi::+:* 10 cells, five larvae; *Repo::Syb-RNAi: 10* cells, five larvae. All panels show mean ± s.e.m.

Figure 3:

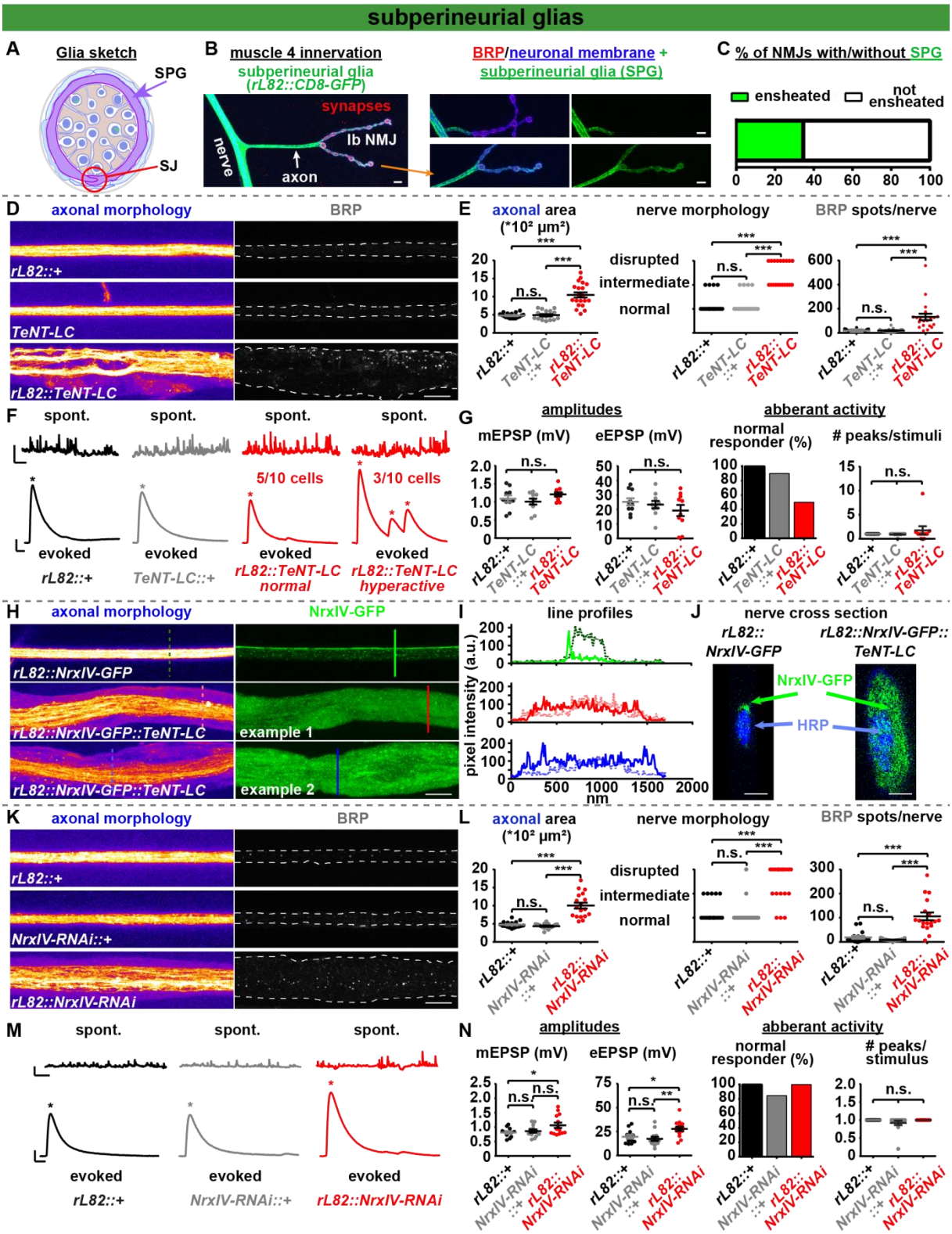

Figure 3: TeNT-LC action in SPGs disrupts axonal transport, causes nerve disintegration, hyperactivity and impairs SJ formation. A Cross section sketch of glial ensheathed motoneuron axon highlighting SPGs (purple). Red circle highlights septate junction (SJ). **B,C** Examples of muscle 4 NMJs of segments A2–A4 from 3rd-instar larvae expressing CD8-GFP in SPGs (left) with (left &

bottom) and without (right top) SPG ensheathment of the NMJ. **C** Quantification of % of NMJs with/without SPG ensheatment. **D,E** Nerves of segments A2–A4 (D) and quantification of axonal area, nerve morphology and BRP spots per nerve (E) from 3rd-instar larvae of *rL82::+* (black), *TeNT-LC::+* (grey) and *rL82::TeNT-LC* (red) animals. Dashed line in D indicates nerve area. **F,G** Representative mEPSP (spont.) and eEPSP (evoked) traces (F; for rl82::TeNT-LC a one normal and one hyperactive trace is shown) and quantification of mEPSP/eEPSP amplitudes, % of recorded cells displaying normal activity (single eEPSP in response to single stimulation) and the normalized number of response peaks per stimulus in *rL82::+* (black), *TeNT-LC::+* (grey) and *rL82::TeNT-LC* (red) animals (G). Asterisks indicate postsynaptic response peaks (eEPSP). **H-J** Nerves of segments A2–A4 (H), vertical line profiles across nerve NrxIV-GFP signals (I; solid line GFP signal, dashed line HRP signal) and orthogonal nerve cross section (J) from 3rd-instar larvae of *rL82::NrxIV-GFP* and *rL82::NrxIV-GFP::TeNT* (two examples are shown). Lines in H indicate line profile positions shown in I. **K-N** Same as in D-G but for *rL82::+* (black), *NrxIV-RNAi::+* (grey) and *rL82::NrxIV-RNAi* (red) animals. Scale bars: (B) 5 µm; (D,H,K) 10 µm; (J) 2.5 µm; (F) mEPSP: 1 s, 2 mV; eEPSP: 25 ms, 5 mV. Statistics: nonparametric one-way analysis of variance (ANOVA) test, followed by Tukey's multiple comparison test except for (E; L: nerve morphology) where a nonparametric Kruskal-Wallis test was performed. ***$p \leq 0.001$; **$p \leq 0.01$; *$p \leq 0.05$; n.s. (not significant) $p > 0.05$. (B,C) 26 NMJs, seven larvae; (D,E) *rL82::+:* 18 nerves, six larvae; *TeNT::+:* 17 nerves, four larvae; *rL82::TeNT:* 20 nerves, six larvae; (F,G) *rL82::+:* 10 cells, five larvae; *TeNT::+:* 10 cells, five larvae; *rL82::TeNT:* 10 cells, five larvae; (H-J) *rL82::NrxIV-GFP:* 18 nerves, six larvae; *rL82::NrxIV-GFP::TeNT:* 18 nerves, six larvae; (K,L) *rL82::+:* 17 nerves, six larvae; *NrxIV-RNAi::+:* 17 nerves, six larvae; *rL82::NrxIV-GFP:* 18 nerves, six larvae; (M,N) *rL82::+:* 12 cells, seven larvae; *NrxIV-RNAi::+:* 13 cells, seven larvae; *rL82::NrxIV-GFP:* 14 cells, seven larvae. All panels show mean ± s.e.m.

Expanded view figure 1 (Fig. EV1):

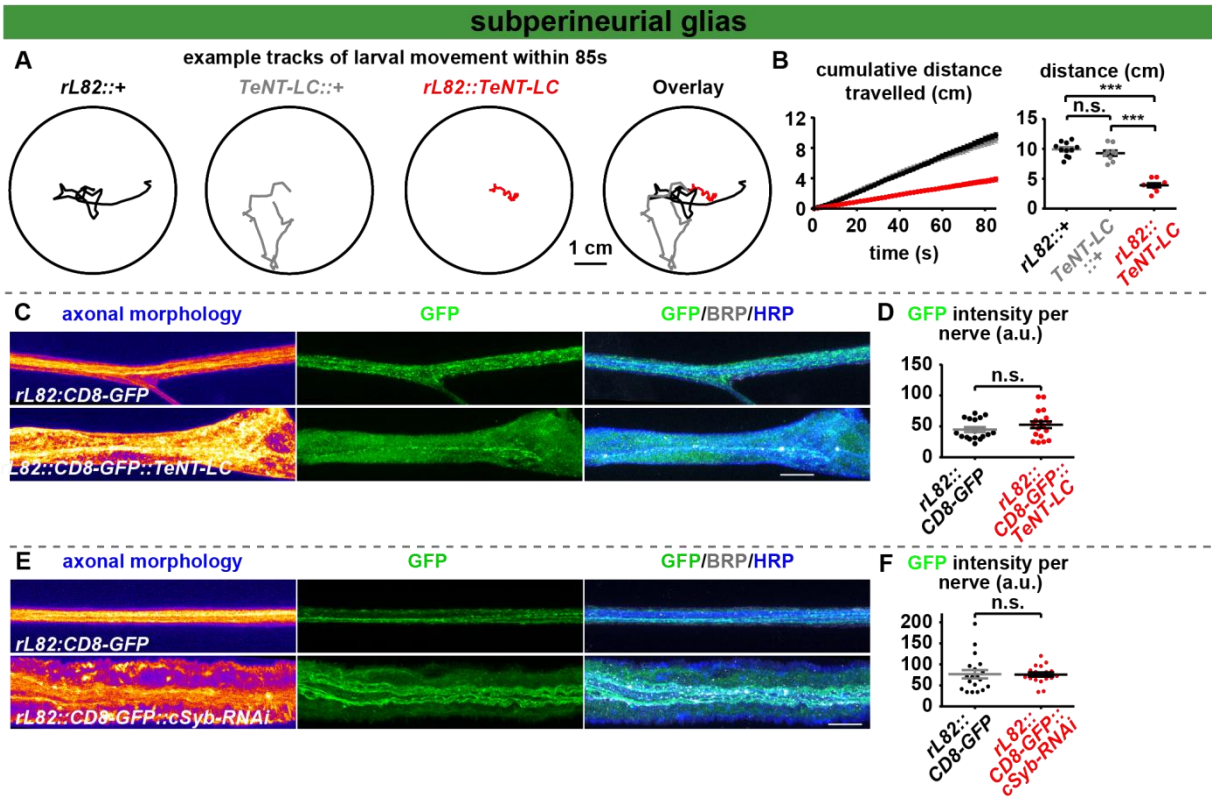

Expanded view figure 1 (Fig. EV1): TeNT-LC expression in SPGs impairs larval movement but does not kill SPG cells. A,B Analysis of larval movement with example tracks over 85s (A), distances travelled over time (85s; B, left) and comparison of final distances travelled by larvae of the indicated genotypes (B, right). See also Videos 4, 2, 5. TeNT-LC data (Video 2) was replotted from Fig. 1C,D. **C,D** Nerves of segments A2–A4 (C) and quantification of GFP intensity per nerve area (D) from 3rd-instar larvae of *rL82::CD8-GFP* (black) and *rL82::CD8-GFP::TeNT-LC* (red) animals. **E,F** same as in C,D but for *rL82::syb-RNAi* (black) and *rL82::CD8-GFP::Syb-RNAi* (red) animals. Scale bars: (A) 1 cm; (C,E) 10 µm. Statistics: nonparametric one-way analysis of variance (ANOVA) test, followed by Tukey's multiple comparison test (A), Student's t test (B) and Mann-Whitney U test (C). ***$p \leq 0.001$; **$p \leq 0.01$; *$p \leq 0.05$; n.s. (not significant) $p > 0.05$. (A,B) *rL82::+:* nine larvae; *TeNT::+:* nine larvae; *rL82::TeNT:* 11 larvae; (C,D) *rl82::CD8-GFP*: 17 nerves, six larvae; *rl82::CD8-GFP::TeNT*: 18 nerves, six larvae; (E,F) *rl82::CD8-GFP*: 19 nerves, six larvae; *rl82::CD8-GFP::Syb-RNAi*: 18 nerves, six larvae. All panels show mean ± s.e.m.

Expanded view figure 2 (Fig. EV2):

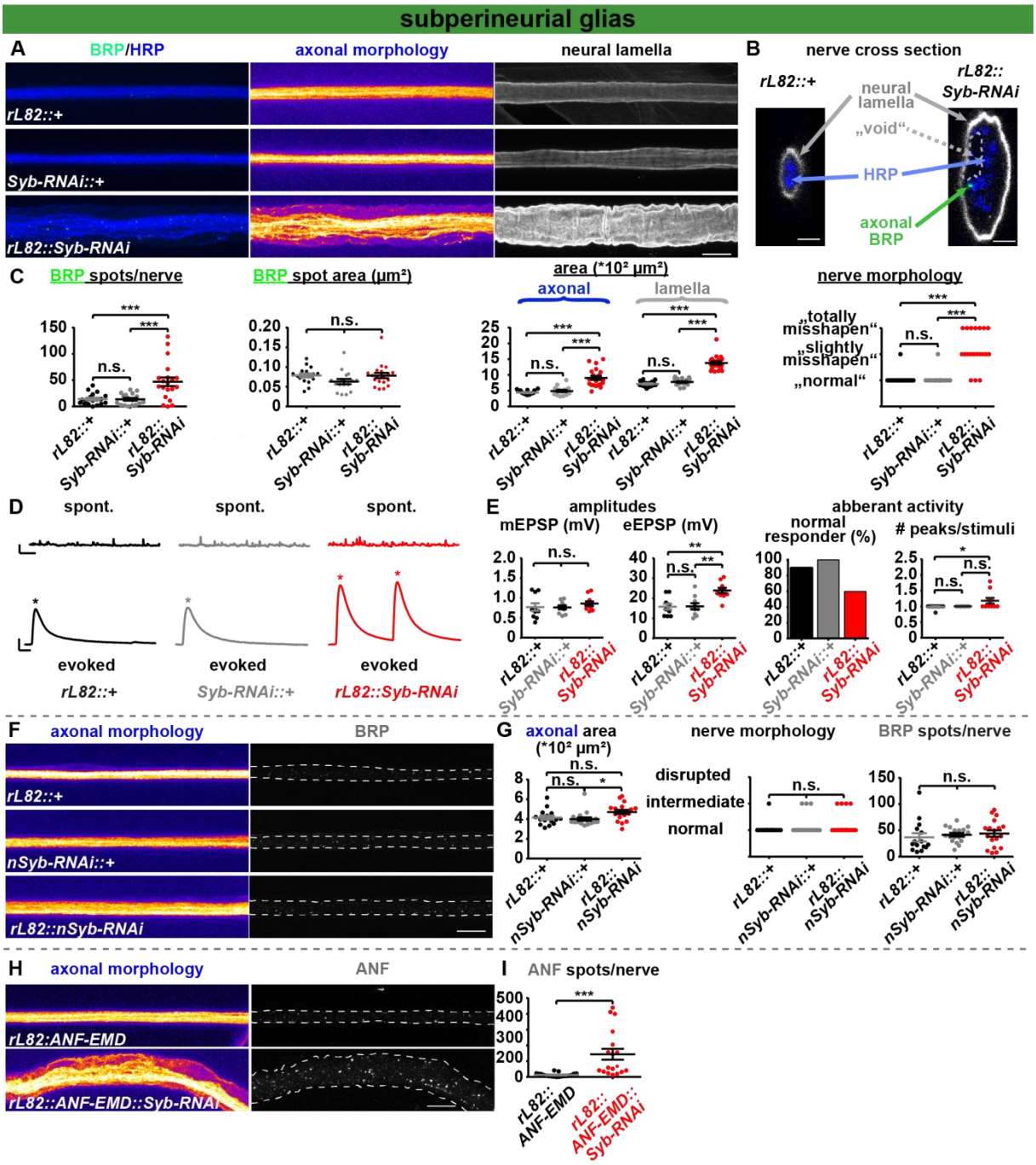

Expanded view figure 2 (Fig. EV2). Syb is targeted by TeNT-LC in SPGs. A,B Nerves of segments A2–A4 (A; neural lamella visualized via GluRIID staining), orthogonal nerve cross section (B) and quantification of BRP spots per nerve, axonal BRP spot area, axonal/lamella area and nerve morphology (C) from 3rd-instar larvae of *rL82::+* (black), *Syb-RNAi::+* (grey) and *rL82:: Syb-RNAi* (red) animals. **D,E** Representative mEPSP (spont.) and eEPSP (evoked) traces (D) and quantification of mEPSP/eEPSP amplitudes, % of recorded cells displaying normal activity and the normalized number of response peaks per stimulus (E) of *rL82::+* (black), *Syb-RNAi::+* (grey) and *rL82:: Syb-RNAi* (red) animals (G). Asterisks indicate postsynaptic response peaks (eEPSP). **F,G** Nerves of

segments A2–A4 (F) and quantification of axonal area, nerve morphology and BRP spots per nerve (G) from 3rd-instar larvae of *rL82::+* (black), *nSyb-RNAi::+* (grey) and *rL82::nSyb-RNAi* (red) animals. Dashed lines indicate nerve areas. **H,I** Nerves of segments A2–A4 (H) and quantification of ANF spots per nerve (I) from 3rd-instar larvae of *rL82::ANF-EMD* (black) and *rL82::ANF-EMD::TeNT* (red) animals. Scale bars: (A, F, H) 10 µm; (B) 2.5µm; (D) mEPSP: 1 s, 2 mV; eEPSP: 25 ms, 5 mV. Statistics: nonparametric one-way analysis of variance (ANOVA) test, followed by Tukey's multiple comparison test except for (C,G: nerve morphology) where a nonparametric Kruskal-Wallis test and (I) where a Student's t test was performed. ***$p \leq 0.001$; **$p \leq 0.01$; *$p \leq 0.05$; n.s. (not significant) $p > 0.05$. (A-C) *rl82::+*: 18 nerves, six larvae; *Syb-RNAi::+*: 17 nerves, six larvae; *rL82::Syb-RNAi*: 20 nerves, six larvae; (D,E) *rl82::+*: 10 cells, five larvae; *Syb-RNAi::+*: 10 cells, five larvae; *rL82::Syb-RNAi*: 10 cells, five larvae; (F,G) *rl82::+*: 15 nerves, five larvae; *nSyb-RNAi::+*: 18 nerves, six larvae; *rL82::nSyb-RNAi*: 18 nerves, six larvae; (H,I) *rL82::ANF-EMD*: 19 nerves, six larvae; *rL82::ANF-EMD::Syb-RNAi*: 18 nerves, six larvae. All panels show mean ± s.e.m.

Figure 4:

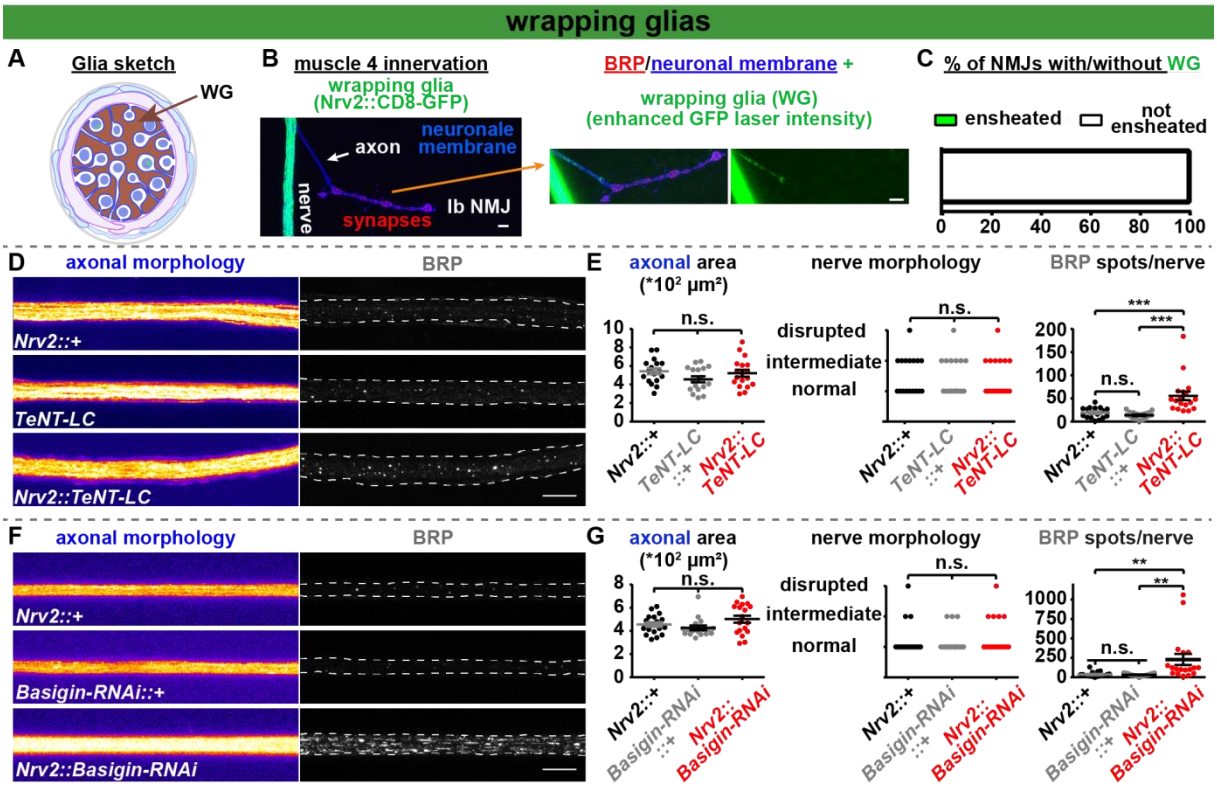

Figure 4: TeNT-LC action in WGs causes axonal BRP accumulation similarly to Basigin-KD. **A** Cross section sketch of glial ensheathed motoneuron axon highlighting WGs (brown). **B,C** Example of muscle 4 NMJs of segments A2–A4 from 3rd-instar larvae expressing CD8-GFP in WGs (left) with enhanced GFP laser intensity (right). **C** Quantification of % of NMJs with/without WG ensheatment. **D,E** Nerves of segments A2–A4 (D) and quantification of axonal area, nerve morphology and BRP spots per nerve (E) from 3rd-instar larvae of *Nrv2::+* (black), *TeNT-LC::+* (grey) and *Nrv2::TeNT-LC* (red) animals. Dashed line in D indicates nerve area. **F,G** Same as in D,E but for *Nrv2::+* (black), *Basigin-RNAi::+* (grey) and *Nrv2::Basigin-RNAi* (red) animals. Scale bars: (B) 5 µm; (D,F) 10 µm. Statistics: nonparametric one-way analysis of variance (ANOVA) test, followed by Tukey's multiple comparison test except for (E; G: nerve morphology) where a nonparametric Kruskal-Wallis test was performed. ***$p \leq 0.001$; n.s. (not significant) $p > 0.05$. (B,C) 23 NMJs, six larvae; (D, E) *Nrv2::+*: 17 nerves, six larvae; *TeNT::+:* 17 nerves, six larvae; *Nrv2::TeNT*: 18 nerves, six larvae; (F,G) *Nrv2::+*: 17 nerves, six larvae; *Basigin-RNAi::+:* 17 nerves, five larvae; *Nrv2::Basigin-RNAi*: 18 nerves, six larvae. All panels show mean ± s.e.m.

Expanded view figure 3 (Fig. EV3):

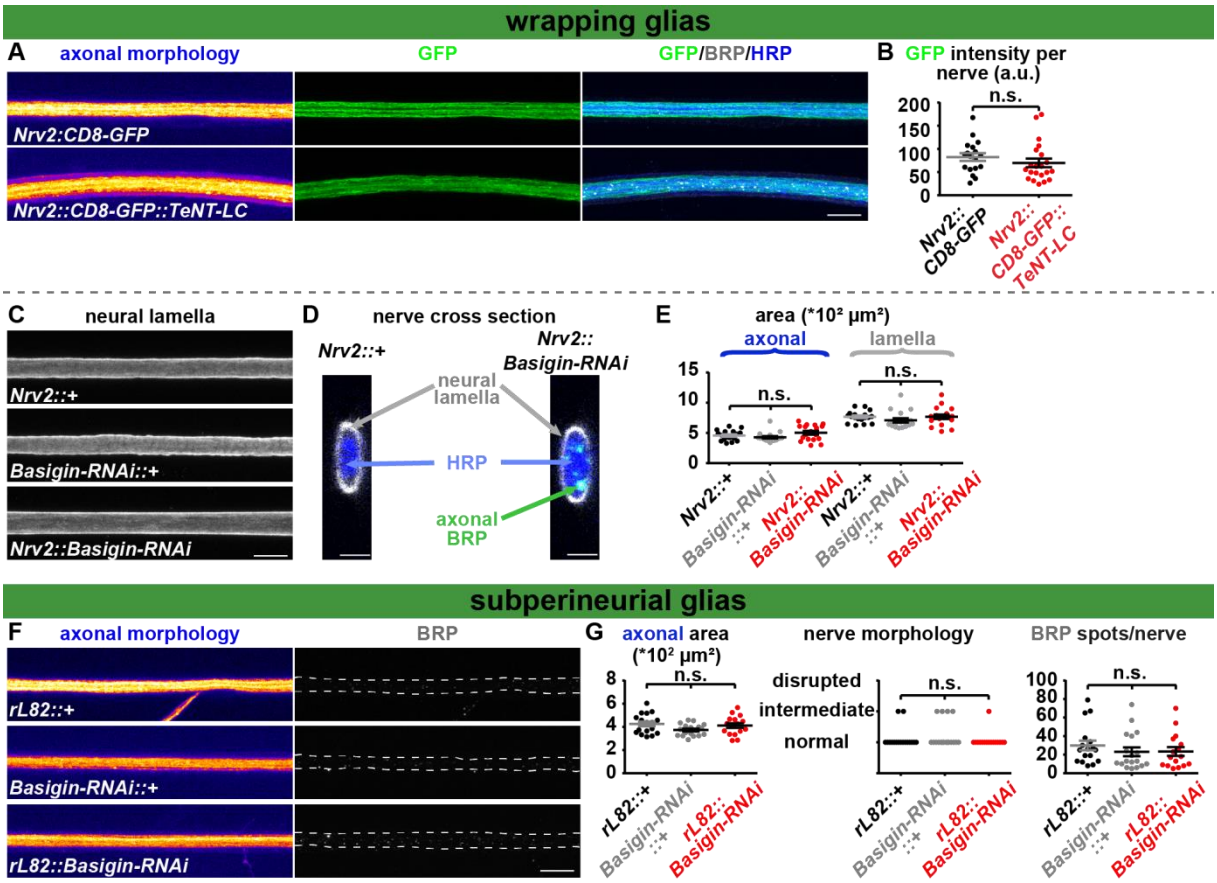

Expanded view figure 3 (Fig. EV3). WGs support axonal transport. A,B Nerves of segments A2–A4 (A) and quantification of GFP intensity per nerve area (B) from 3rd-instar larvae of *Nrv2::CD8-GFP* (black) and *Nrv2::CD8-GFP::TeNT-LC* (red) animals. **C-E** Nerves of segments A2–A4 (C; neural lamella visualized via GluRIID staining), orthogonal nerve cross section (D) and quantification of axonal/lamella area (E) from 3rd-instar larvae of *Nrv2::+* (black), *Basigin-RNAi::+* (grey) and *Nrv2::Basigin-RNAi* (red) animals. **F-G** Nerves of segments A2–A4 (F) and quantification of axonal area, nerve morphology and BRP spots per nerve (G) from 3rd-instar larvae of *rL82::+* (black), *Basigin-RNAi::+* (grey) and *rL82::Basigin-RNAi* (red) animals. Scale bars: (A, C, F) 10 µm; (D) 2.5 µm. Statistics: nonparametric one-way analysis of variance (ANOVA) test, followed by Tukey's multiple comparison test except for (G, nerve morphology) where a nonparametric Kruskal-Wallis test was performed and (B) where a Mann-Whitney U Test was performed. ***$p \leq 0.001$; **$p \leq 0.01$; *$p \leq 0.05$; n.s. (not significant) $p > 0.05$. (A,B) *Nrv2::CD8-GFP*: 18 nerves, six larvae; *Nrv2::CD8-GFP::TeNT*: 21 nerves, six larvae; (C-E) *Nrv2::+*: 17 nerves, six larvae; *Basigin-RNAi::+:* 17 nerves, five larvae; *Nrv2::Basigin-RNAi*: 18 nerves, six larvae; (F,G) *rL82::+*: 17 nerves, six larvae; *Basigin-RNAi::+:* 18 nerves, six larvae; *rL82::Basigin-RNAi*: 18 nerves, six larvae. All panels show mean ± s.e.m.